

RadHARSimulator V2: Video to Doppler Generator

Weicheng Gao , Graduate Student Member, IEEE

Abstract—Radar-based human activity recognition (HAR) lies in providing decision-making insights for urban warfare and counter-terrorism through contactless perception, while safeguarding privacy and security in areas such as monitoring for elderly individuals living alone and smart home applications. However, this field still lacks a comprehensive simulation method for radar-based HAR. Existing software is developed based on models or motion-captured data, resulting in limited flexibility. To address this issue, a simulator that directly generates Doppler spectra from recorded video footage (RadHARSimulator V2) is presented in this paper. Both computer vision and radar modules are included in the simulator. In computer vision module, the real-time model for object detection with global neighbor is first used to detect and track human targets in the video. Then, the high-resolution network is used to estimate two-dimensional poses of the detected human targets. Next, the three-dimensional poses of the detected human targets are obtained by nearest matching method. Finally, smooth temporal three-dimensional pose estimation is achieved through Kalman filtering. In radar module, pose interpolation and smoothing are first achieved through the Savitzky-Golay method. Second, the delay model and the mirror method are used to simulate echoes in both free-space and through-the-wall scenarios. Then, range-time map is generated using pulse compression, moving target indication, and DnCNN. Next, Doppler-time map (DTM) is generated using short-time Fourier transform and DnCNN again. Finally, the ridge features on the DTM are extracted using the maximum local energy method. In addition, a hybrid parallel-serial neural network architecture is proposed for radar-based HAR. Numerical experiments are conducted and analyzed to demonstrate the effectiveness of the designed simulator and the proposed network model. The open-source code of this work can be found in: [GitHub/JoeyBGOfficial/RadHARSimulatorV2](https://github.com/JoeyBGOfficial/RadHARSimulatorV2)

Index Terms—radar signal processing, human activity recognition, micro-Doppler signature, computer vision, neural networks.

I. INTRODUCTION

IN recent years, as a non-contact sensing technique, radar-based human activity recognition (HAR) has become a research hotspot in both academia and industry [1]–[5]. Its main benefit is that it makes it possible for intelligent perception to function continuously without being impacted by lighting or violating people’s privacy [6]–[9]. This field is rapidly developing from a cutting-edge academic issue to large-scale practical applications, positioned to become an

Manuscript received XXXXXXXX XX, 2025; revised XXXXXXXX XX, 2025; accepted XXXXXXXX XX, 2025. Date of publication XXXXXXXX XX, 2025; date of current version XXXXXXXX XX, 2025.

My Bio: My name is Weicheng Gao. I’m a Ph.D. student from Beijing Institute of Technology. I’m majored and interested in mathematical and modeling theory research of signal processing, radar signal processing techniques, and AI for radar, apprenticed under professor Xiaopeng Yang. I’m currently dedicated in the field of Through-the-Wall Radar Human Activity Recognition. Looking forward to learning and collaborating with more like-minded teachers and mates. (e-mail: JoeyBG@126.com).

Digital Object Identifier 10.48550/arXiv.2511.XXXXXX.



Fig. 1. Splash screen of RadHARSimulator V2.

essential weapon in effective warfare and terrorist operations, as well as to build an intelligent, user-friendly, and privacy-secure social infrastructure [10]–[12].

Research in radar-based HAR spans over two decades, encompassing progressive levels of development such as human body models, statistical learning methods based on manual feature selection, and deep learning approaches utilizing automatic feature extraction [13]. However, research in this field was accelerated significantly five years ago, with an increasing number of researchers and institutions dedicating resources to developing more precise and cost-effective methods in hopes of enhancing their practical value [14], [15]. Among them, a method combining an improved principal component analysis and an improved VGG-16 model was proposed by Zhao et Al. to solve the problem of over-fitting caused by the small-scale dataset, and an accuracy of 96.34% on HAR was achieved [16]. A time-distributed convolutional neural network (CNN) enhanced with a bidirectional long-short term memory (Bi-LSTM) mechanism was used by Singh et Al. to classify five human full-body activities, and an accuracy of 90.47% was achieved [17]. A real-time human activity recognition method for through-the-wall (TTW) radar was proposed by Cheng et Al. to solve the problem of unknown temporal allocation of activities during recognition, and an average accuracy of 97.6% was achieved [18]. A hybrid CNN-LSTM network was used by Zhu et Al. to classify human activities based on micro-Doppler radar, and an accuracy of 98.28% was achieved

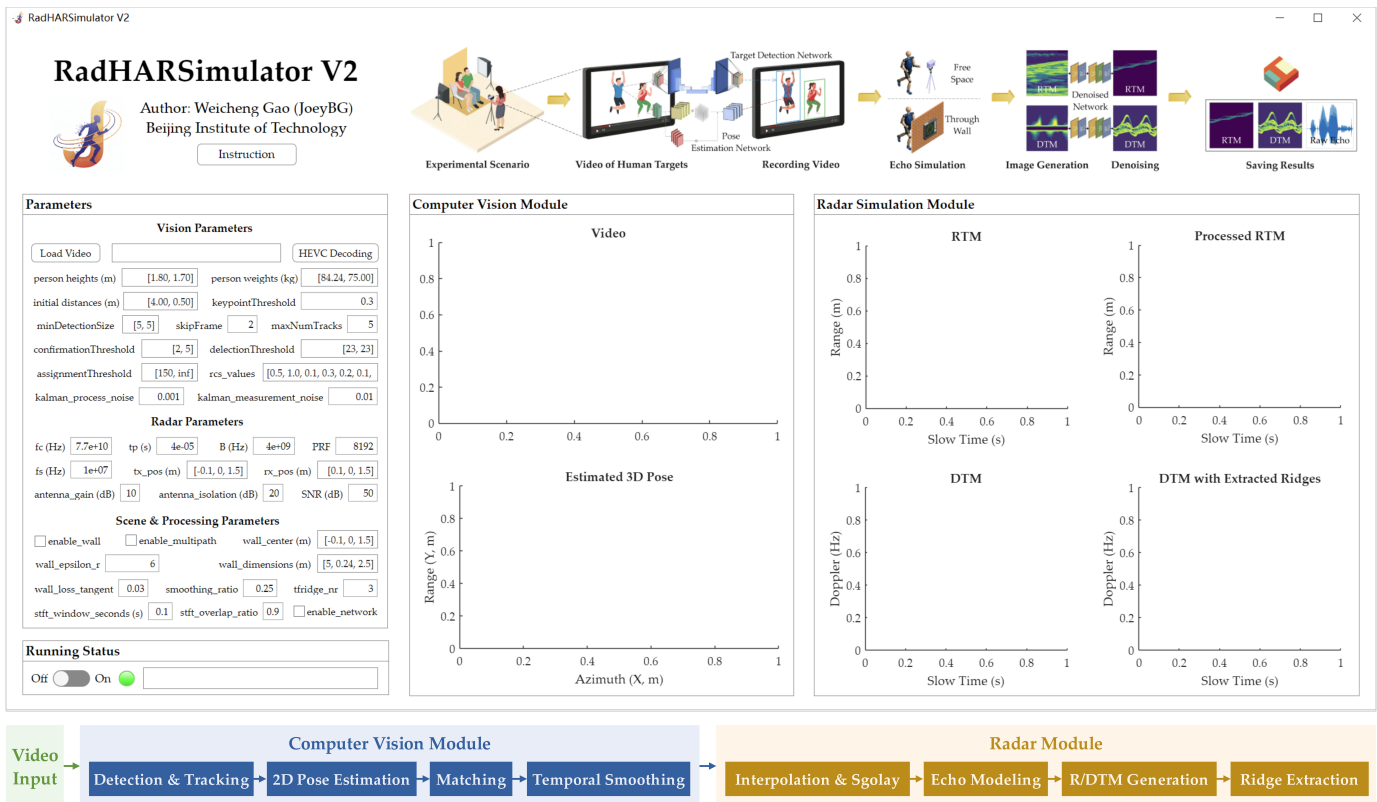


Fig. 2. The interface and processing overflow of RadHARSimulator V2.

[19]. The problem that deploying an HAR model in unseen environments remains challenging was solved by El Hail et Al. by applying data augmentation and unsupervised domain adaptation to enhance the robustness of HAR models, and the F1-score was improved by 0.281 with data augmentation and by 0.337 when the DANN strategy was jointly used with data augmentation [20]. A method of a two-stream one-dimensional CNN with a bidirectional gated recurrent unit was proposed by Tan et Al. to recognize six daily activities, and an impressive accuracy rate of 98.2% was achieved [21]. A stacked recurrent neural network (RNN) was used by Wang et Al. to recognize human motion, and an accuracy of 92.65% was achieved [22]. A Bi-LSTM network was used by Li et Al. to multimodal continuous HAR and fall detection, and an accuracy of over 95% was achieved [23]. LSTM was used by Noori et Al. for the static actions with a non-wearable ultra-wideband (UWB) radar, and an accuracy approaching 99.6% was achieved [24]. Frequency-modulated continuous wave radar systems were studied by Pesin et Al. for radar-based HAR, and an average classification accuracy of 89.8% for the millimeter wave radar system and 95.7% for the sub-6 GHz radar was achieved [25]. A deep convolutional autoencoder was used by Seyfioglu et Al. for radar-based classification of similar aided and unaided human activities, and the highest accuracy of 94.2% was achieved [26]. A multi-frequency spectrograms was used by Ding et Al. to continuous human activity recognition through parallelism LSTM, and accuracies of 85.41% and 96.15% were achieved [27]. An open source pretrained CNN was used by Chakraborty et Al. to train with their own provided dataset, and an overall accuracy of 98% was achieved [28].

A Transformer was trained as an end-to-end model and used for the classification of seven coarse-scaled tasks by Yan et Al., and the accuracy of the Transformer was the highest at 90.45% [29]. A comparative study on recent progress of machine learning-based HAR with radar was performed by Papadopoulos and Jelali, and the CNN-based classification achieved better performance in comparison to the investigated RNN-based methods [30]. Our team also conducted relevant researches, primarily focusing on the TTW scenario, including achieving data augmentation [31], higher recognition accuracy and robustness [32], faster inference speeds [33], improved kinematic models [34], enhanced feature extraction [35], and better generalization for targets with varying body types [36]. These works, being focused on the design of intelligent algorithms, invariably required the optimization or training of a certain amount of prior data. For the pre-verification phase of algorithms, generating large amounts of echoes or spectra using simulation methods is a necessary area of research.

Not long ago, RadHARSimulator V1, a model-based radar HAR simulator integrating an anthropometrically scaled 13-scatterer kinematic model to simulate 12 activities is developed [37], generating radar echoes with dynamic radar cross-section, propagation effects, and noise, processing data through a pipeline to produce range-time map (RTM) and Doppler-time map (DTM). However, shortcomings are exhibited, including limited waveform and radar support, simplistic models omitting complex motions and multipath, and insufficient user testing. Therefore, methods for generating radar echoes and spectra from recorded videos are deemed necessary, as they capture real-world visual cues with pose

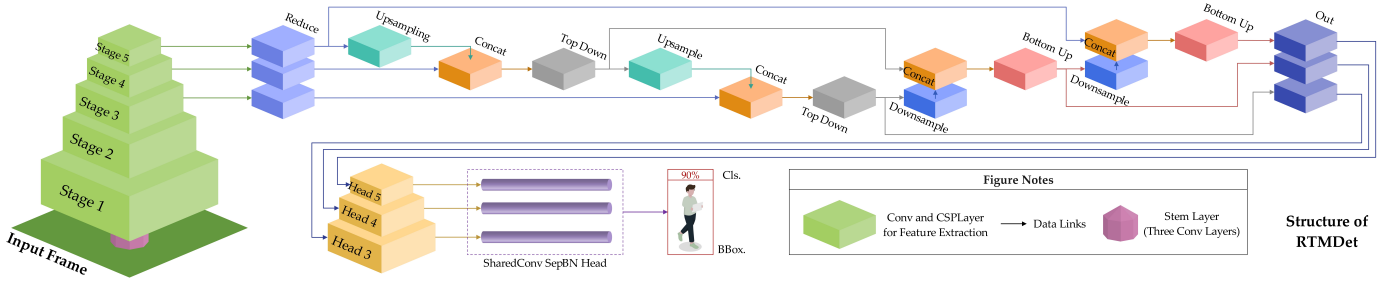


Fig. 3. Structure design of the RTMDet for detecting human targets in video frames.

variations, enhancing simulation realism, diversity, and applicability for challenging HAR beyond analytical models.

Taking all the above considerations into account, RadHAR-Simulator V2, a simulator for generating radar echoes and spectra from recorded video footage is proposed in this paper, shown in Fig. 2. Specific contributions of this paper are:

(1) Three-Dimensional (3D) Human Pose and Location Estimation: First, real-time model for object detection (RTMDet) is employed for video human detection, while the global nearest neighbor (GNN) method is utilized for human tracking. Subsequently, high-resolution network (HRNet) is applied to perform two-dimensional (2D) pose estimation of detected human targets. Next, the nearest matching method is used to achieve 3D pose estimation of human targets. Finally, the geometric parameters derived from the 3D poses are leveraged to estimate the spatial locations of all human joints.

(2) Temporal Pose Smoothing: The Kalman filter method is employed to achieve temporal consistency and smoothing in human 3D pose and location estimation.

(3) Visual-to-Radar Pose Interaction: Linear interpolation method and Savitzky-Golay filtering technique are employed to achieve pose interaction between video frame rates and radar pulse repetition frequency (PRF), along with second-order smoothing.

(4) Radar Spectra Generation and Enhancement: Both free-space and TTW scenarios are introduced, with radar echo generation and multipath effect simulation implemented based on delay models and mirroring methods. Pulse compression and moving target indication (MTI) methods are employed to generate the RTM, while the short-time Fourier transform (STFT) method is used to generate the DTM. Additionally, the DnCNN model is utilized to perform denoising and micro-Doppler signature enhancement on both the RTM and DTM, and the ridge features on DTM are extracted using the maximum local energy (MLE) method.

(5) Novel Radar-based HAR Method: a novel hybrid parallel-serial neural network architecture (SPNet) is proposed for radar-based HAR.

Besides, numerical experiments are also conducted in this paper, aiming to evaluate the validity and accuracy of the data generated by the simulator, while simultaneously assessing the effectiveness of the proposed network approach.

The rest of the paper is organized as follows. The computer vision module, which achieves video to 3D pose and location estimation, is presented in section II. The radar module, which

achieves 3D pose to spectra generation and feature extraction, is presented in section III. The design of hybrid parallel-serial neural network model for radar-based HAR is presented in section IV. Numerical experiments, analysis, and discussions are presented in section V. Finally, the conclusion is given in section VI.

II. COMPUTER VISION MODULE

In this section, the RTMDet and GNN-based video human detection and tracking method is first presented. Then, the 2D pose estimation of the detected human targets achieved by HRNet is then discussed. Next, the 3D pose estimation is achieved by nearest matching. Finally, the Kalman filtering method is used to achieve temporal smoothing in human 3D pose and location estimation.

A. Detection and Tracking Human Targets

The detection of human targets in video is achieved by RTMDet. Details can be found in [38]. As shown in Fig. 3, at time t_f , the image frame of the input video is represented as a matrix $\mathbf{I}_{t_f} \in \mathbb{R}^{H \times W \times C}$, where H, W are the width and height of the frame, and C is the number of channels. Some of the data augmentation techniques are taken to produce the network input tensor $\mathbf{X}_{in,t_f} \in \mathbb{R}^{H' \times W' \times C}$. The overall architecture of RTMDet consists of three core components, including the backbone, the neck, and the detection head.

CSPNeXt is adopted as the foundational building module for the backbone network. The network is initiated with a stem layer, followed by four processing stages. The core of the CSPNeXt module is formed by depthwise separable convolutions that utilize large convolution kernels; this design is aimed at extracting image features efficiently.

The neck network is structured on a path aggregation feature pyramid network. Feature maps output from different stages of the backbone network are received and fused through a top-down path followed by a bottom-up path. This process integrates contextual information across multiple scales, thereby enhancing the model's detection capability for targets of varying sizes. The neck network likewise employs CSPNeXt modules to process the feature maps.

A shared detection head is employed by RTMDet to simultaneously handle classification and regression tasks. To enhance efficiency and reduce parameter count, convolutional layer weights are shared across detection heads at different feature levels, while independent batch normalization layers

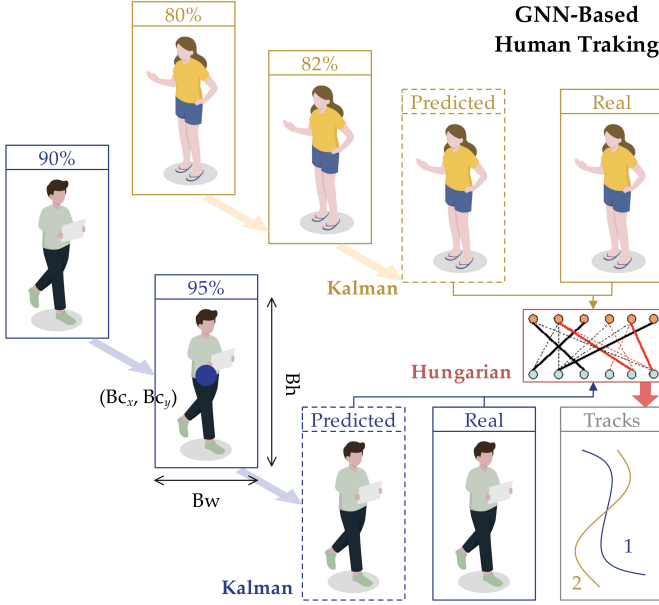


Fig. 4. Human tracking based on GNN.

are maintained for each. This design enables the model to effectively predict object categories and bounding box positions from the fused multi-scale feature maps.

The loss function of RTMDet is composed of two components, including classification loss and bounding box regression loss. Positive and negative samples are determined through a dynamic soft label assignment strategy, and the corresponding losses are computed accordingly. The classification task employs quality focal loss (QFL) $\mathcal{L}_{\text{QFL}}(\cdot)$. Bounding-box localization is performed using generalized intersection over union loss (GIoU) $\mathcal{L}_{\text{GIoU}}(\cdot)$. Complete loss function $\mathcal{L}_{\text{RTMDet}}$ is denoted as follows:

$$\begin{aligned} \mathcal{L}_{\text{RTMDet}} = & \frac{1}{N_{\text{pos}}} \sum_i \mathcal{L}_{\text{QFL}}(\text{Sig}m_i, \text{IoU}_i) \\ & + \frac{\lambda_{\text{RTMDet}}}{N_{\text{pos}}} \sum_i \mathbb{I}_{y_i > 0} \cdot \mathcal{L}_{\text{GIoU}}(\text{BBox}_i, \text{GTB}_i), \end{aligned} \quad (1)$$

where \sum_i is the summation over all prediction samples, N_{pos} represents the total number of samples identified as positive by the passive allocation strategy, λ_{RTMDet} is the weight coefficient for the regression loss, \mathbb{I} is the indicator function, $\text{Sig}m_i$ is the output of the i^{th} prediction sample after activation by the Sigmoid function, IoU_i is the true label IoU for the i^{th} prediction sample, BBox_i is the bounding box coordinates representing the prediction for the i^{th} positive sample, and GTB_i is the coordinates of the true target bounding box matched with the i^{th} positive sample.

At frame t_f , the RTMDet outputs a set of bounding box matrices $\mathbf{X}_{\text{Box},t_f} = [\mathbf{X}_{\text{Box},1,t_f}, \mathbf{X}_{\text{Box},2,t_f}, \dots, \mathbf{X}_{\text{Box},P,t_f}]$, where each $\mathbf{X}_{\text{Box},p,t_f}$, $p \in \mathbb{Z}^+ \cap [1, P]$ corresponds to a detected potential p^{th} human target, which will be used for subsequent GNN tracking.

Assume at $t_f - \Delta t_f$, M valid tracks have been recorded: $\mathbf{Tr}_{t_f - \Delta t_f} = [\mathbf{Tr}_{1,t_f - \Delta t_f}, \mathbf{Tr}_{2,t_f - \Delta t_f}, \dots, \mathbf{Tr}_{M,t_f - \Delta t_f}]$. The state of each track $\mathbf{Tr}_{m,t_f - \Delta t_f}$, $m \in \mathbb{Z}^+ \cap [1, M]$ can be

represented by a vector \mathbf{st}_m , $m \in \mathbb{Z}^+ \cap [1, M]$ including both position and velocity information, defined as:

$$\mathbf{st}_m = [\text{B}c_x, \text{B}c_y, \text{B}w, \text{B}h, \dot{\text{B}}c_x, \dot{\text{B}}c_y, \dot{\text{B}}w, \dot{\text{B}}h]^\top, \quad (2)$$

where $\text{B}c_x, \text{B}c_y$ are center coordinates of the bounding box, $\text{B}w, \text{B}h$ are the width and height of the bounding box, respectively, and $\dot{\cdot}$ means the first derivative of a variable. To match these tracks with the current frame's detection, each track's position at the current frame t_f must first be predicted. Here, a linear motion model is adopted:

$$\hat{\mathbf{st}}_{m,t_f} = \mathbf{TransF} \cdot \mathbf{st}_{m,t_f - \Delta t_f}, \quad (3)$$

where \mathbf{TransF} is the state transition matrix:

$$\mathbf{TransF} = \begin{bmatrix} \mathbf{I}_{4 \times 4} & \Delta t_f \cdot \mathbf{I}_{4 \times 4} \\ \mathbf{0}_{4 \times 4} & \mathbf{I}_{4 \times 4} \end{bmatrix}, \quad (4)$$

where \mathbf{I} is the identity matrix. Through this, the prediction bounding box $\hat{\mathbf{X}}_{\text{Box},m,t_f}$, $m \in \mathbb{Z}^+ \cap [1, M]$ for each track in the current frame is obtained.

Calculate the IoU between the predicted bounding box $\hat{\mathbf{X}}_{\text{Box},m,t_f}$ and the detected bounding box $\mathbf{X}_{\text{Box},p,t_f}$:

$$\begin{aligned} \text{IoU}(m,p) &= \frac{\text{Area}(\hat{\mathbf{X}}_{\text{Box},m,t_f} \cap \mathbf{X}_{\text{Box},p,t_f})}{\text{Area}(\hat{\mathbf{X}}_{\text{Box},m,t_f} \cup \mathbf{X}_{\text{Box},p,t_f}),} \quad (5) \\ \text{cost}_{mp} &= 1 - \text{IoU}(m,p) \end{aligned}$$

where $\text{Area}(\cdot)$ is the area calculation function, and cost_{mp} is the cost element. Combine all cost elements to obtain the cost matrix $\mathbf{cost}_{M \times P}$.

After constructing the cost matrix, the data association problem is transformed into a classic assignment problem, which can be solved in polynomial time using the Hungarian algorithm to find the optimal solution. The objective of the algorithm is to find a binary allocation matrix $\mathbf{Alloc}_{M \times P}$ where an element $\text{alloc}_{mp} = 1$ indicates that track m is matched with detection p , and 0 otherwise. Solve the optimization problem:

$$\begin{aligned} \min & \sum_{m=1}^M \sum_{p=1}^P \text{cost}_{mp} \cdot \text{alloc}_{mp} \\ \text{s.t.} & \sum_{m=1}^M \text{alloc}_{mp} \leq 1, \forall m \in \mathbb{Z}^+ \cap [1, M]. \\ & \sum_{p=1}^P \text{alloc}_{mp} \leq 1, \forall p \in \mathbb{Z}^+ \cap [1, P] \end{aligned} \quad (6)$$

A set of paired matching relationships is obtained. The GNN updates, creates, and deletes tracks based on the assignment results [40]: For successfully matched track-detection pairs (m,p) , use the detection box $\mathbf{X}_{\text{Box},p,t_f}$ information to update the state vector \mathbf{st}_m of track \mathbf{Tr}_m . Simultaneously, reset the track's counter to 0. Detection boxes not assigned to any existing track may represent newly emerging targets. A tentative track is only confirmed as a valid new track if it can be matched consecutively across subsequent frames. For tracks that fail to match any detection box in the current frame, their counter increments by 1. When this counter exceeds a preset threshold, the target is deemed to have left the scene or become completely occluded, and the track is deleted.

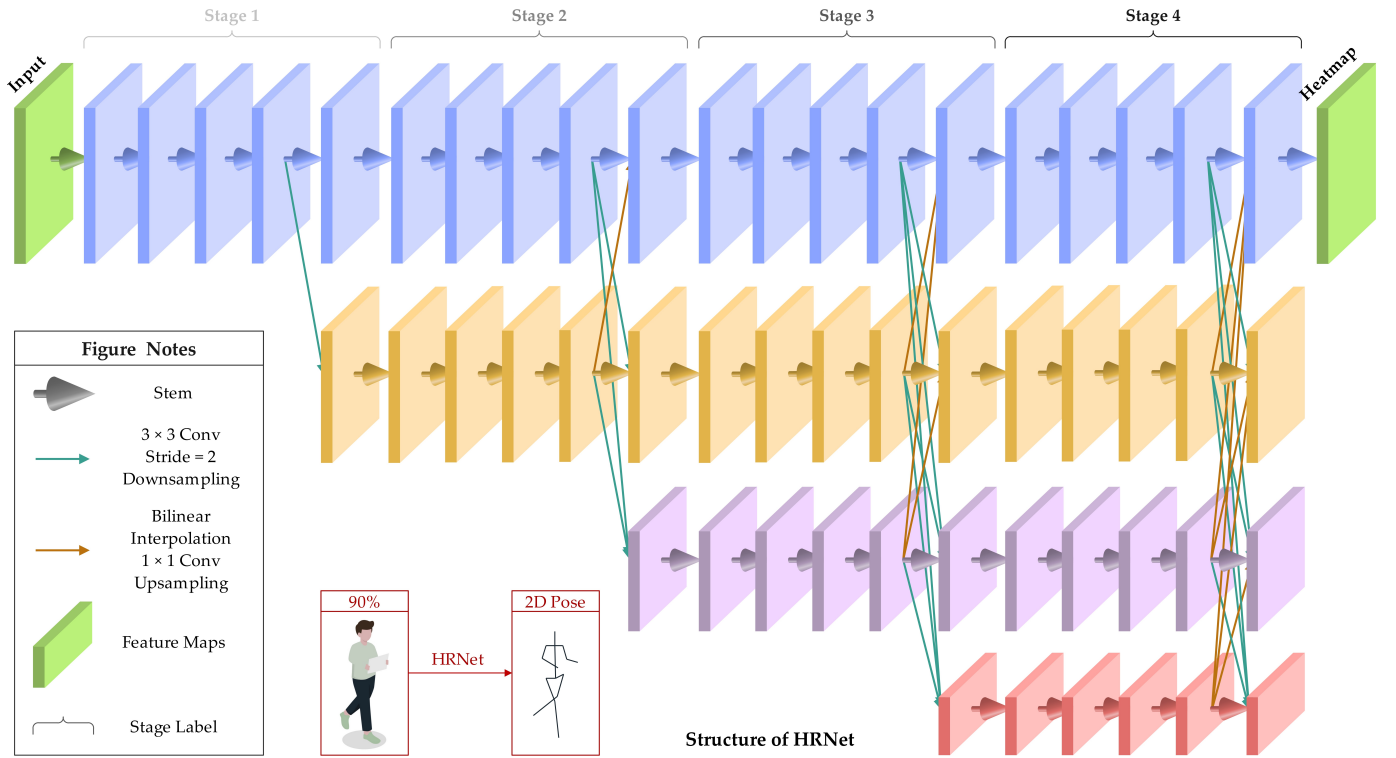


Fig. 5. Structure design of the HRNet for estimating 2D poses of the detected human targets.

Through iterative cycles of above steps, the GNN algorithm provides stable and continuous tracking for human targets within video sequences. The detection box $\mathbf{X}_{\text{Box},t_f}$ for each tracked target will be used for subsequent 2D pose estimation.

B. 2D Pose Estimation

The 2D pose estimation of human targets is achieved by HRNet. Details can be found in [41]. As shown in Fig. 5, high-resolution feature representations are maintained by HRNet throughout the entire network processing, thereby avoiding spatial information loss caused by multiple downsamplings in traditional methods. The input image $\mathbf{X}_{\text{Box},t_f}$ is used as the starting point, where frame time information can serve as a reference for temporal processing, but the network itself primarily focuses on spatial feature extraction. This objective is achieved by HRNet through the parallel connection of multiple resolution subnets, with the initial stage employing a high-resolution subnet to process the input, and lower-resolution subnets being gradually introduced to capture multi-scale contextual information.

The network structure is composed of four stages, each containing a series of convolutional layers and residual blocks. The first stage begins with the high-resolution subnet, where initial features are extracted using convolutional operations. In subsequent stages, lower-resolution subnets are progressively added; these subnets reduce spatial dimensions through strided convolutions while increasing the number of channels to enrich feature representations. A key multi-scale fusion mechanism is performed periodically between different subnets, with information exchanged via upsampling and downsampling operations to ensure effective integration of high-resolution

features with low-resolution semantic contexts. This design ensures that detailed information is always preserved in the high-resolution subnet, while global perception is provided by the low-resolution subnets.

In the output part, feature maps from all subnets are fused by HRNet, ultimately generating a set of heatmaps, each corresponding to the spatial probability distribution of human joints. These heatmaps are predicted from the fused features through convolutional layers and are directly used to infer the positions of human pose joints.

The mean squared error is adopted by the loss function of HRNet, with the objective being to minimize the difference between the joint heatmaps predicted by the network and the ground-truth heatmaps, which is defined as follows:

$$\mathcal{L}_{\text{HRNet}} = \frac{\sum_{k=1}^K \sum_{i=1}^{\text{Bh}} \sum_{j=1}^{\text{Bw}} \|\mathbf{Gauss}_k(i,j) - \hat{\mathbf{Gauss}}_k(i,j)\|_2^2}{N_{\text{HRNet},k} K_{\text{HRNet}}}, \quad (7)$$

where K_{HRNet} is the total number of joints, the number of output joints for HRNet is 17 in this work, and the number of nodes subsequently used for 3D matching is 14, \mathbf{Gauss}_k is the ground-truth Gaussian heatmap corresponding to the k^{th} joint, $\hat{\mathbf{Gauss}}_k$ is the predicted Gaussian heatmap corresponding to the k^{th} joint, and $N_{\text{HRNet},k}$ is the normalized factor set to the sum of all pixel values in the ground-truth heatmap.

The 2D pose obtained from HRNet inference can be expressed as $\mathbf{P}_{2\text{D}} \in \mathbb{R}^{K_{\text{HRNet}} \times 2}$. This result will be used for subsequent mapping from 2D to 3D pose.

C. 2D to 3D Pose Matching

The nearest matching algorithm is employed to implement the mapping from 2D pose to 3D pose [42]. First, extract

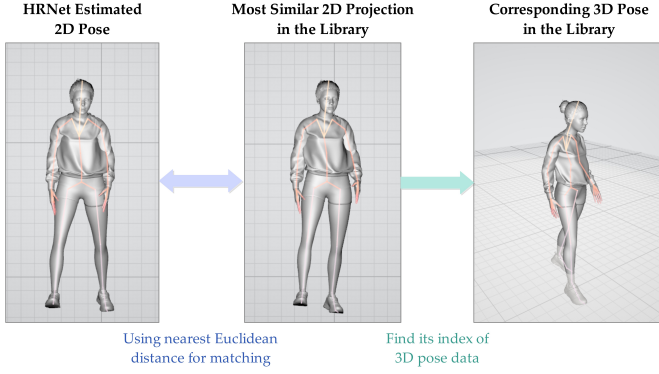


Fig. 6. Schematic of the proposed 2D to 3D pose matching method.

1877420 3D poses from the Human3.6M training dataset [43] and construct the library $\mathbf{Pool}_{3D} \in \mathbb{R}^{N_{H3.6M} \times K_{HRNet} \times 3}$, where $N_{H3.6M}$ is the total number of data in the library. The depth axis of the 3D poses in this library is then pooled to obtain their 2D mappings, forming $\mathbf{Pool}_{2D} \in \mathbb{R}^{N_{H3.6M} \times K_{HRNet} \times 2}$. The pose data in the library is derived from diverse human motion and normalized to unit scale.

To find the best-matching 3D pose of the \mathbf{P}_{2D} , the Euclidean distance between \mathbf{P}_{2D} and each data in library \mathbf{Pool}_{2D} is calculated:

$$d_{\text{pose},i} = \|\mathbf{P}_{2D} - \mathbf{Pool}_{2D}^i\|_2, \quad i \in \mathbb{Z}^+ \cap [1, N_{H3.6M}]. \quad (8)$$

The index i^* of the nearest matching is selected as:

$$i^* = \arg \min_i d_{\text{pose},i}. \quad (9)$$

The corresponding 3D pose is then retrieved as $\mathbf{P}_{3D} = \mathbf{Pool}_{3D}^{i^*}$. To convert the library-derived 3D pose into metric units, a scaling factor based on the human's predefined height and the observed skeletal length in pixels is applied. First, compute the current pixel height h_{pixel} of the skeleton as:

$$h_{\text{pixel}} = \max(\mathbf{P}_{2D}(:,2)) - \min(\mathbf{P}_{2D}(:,2)). \quad (10)$$

Given the human's real-world height h_{real} in meters, the primary scaling factor is $\alpha_{\text{hum}} = \frac{h_{\text{real}}}{h_{\text{pixel}}}$. This factor scales the 2D keypoints in the image plane (X,Z-axes):

$$\mathbf{P}_{\text{meters,orig,xz}} = \mathbf{P}_{2D} \cdot \alpha_{\text{hum}}. \quad (11)$$

For the depth dimension (Y-axis), a reduced scaling is employed to maintain realistic body proportions. Human body depth is typically a fraction of height, thus a depth ratio $\beta_{\text{hum}} = 0.2$ is introduced, assuming depth is approximately 20% of height. The depth $\mathbf{P}_{3D}(:,3)$ is first centered around their mean $\mathbf{P}_{3D}(:,3)$ to avoid offsets:

$$\mathbf{P}_{3D,\text{depth,centered}} = \mathbf{P}_{3D}(:,3) - \overline{\mathbf{P}_{3D}(:,3)}. \quad (12)$$

The scaled depth is then:

$$\mathbf{P}_{\text{meters,orig,y}} = \mathbf{P}_{3D,\text{depth,centered}} \cdot \alpha_{\text{hum}} \cdot \beta_{\text{hum}}. \quad (13)$$

The initial metric pose combines these components:

$$\mathbf{P}_{\text{meters,orig}} = [\mathbf{P}_{\text{meters,orig,xz}}, \mathbf{P}_{\text{meters,orig,y}}]. \quad (14)$$

To anchor the pose in a global metric coordinate system,

the absolute position using the hip center as a reference is tracked. The hip center in the original metric pose is:

$$\mathbf{Hip}_{\text{orig}} = \begin{bmatrix} \overline{\mathbf{P}_{\text{meters,orig}}([9,12],1)}, \overline{\mathbf{P}_{\text{meters,orig}}([9,12],2)}, \\ \overline{\mathbf{P}_{\text{meters,orig}}([9,12],3)} \end{bmatrix}. \quad (15)$$

The relative pose is computed by subtracting this center:

$$\begin{aligned} \mathbf{P}_x^{\text{rel}} &= \mathbf{P}_{\text{meters,orig}}(:,1) - \mathbf{Hip}_{\text{orig}}(1) \\ \mathbf{P}_y^{\text{rel}} &= \mathbf{P}_{\text{meters,orig}}(:,3) - \mathbf{Hip}_{\text{orig}}(3) \\ \mathbf{P}_z^{\text{rel}} &= -(\mathbf{P}_{\text{meters,orig}}(:,2) - \mathbf{Hip}_{\text{orig}}(2)) \end{aligned}. \quad (16)$$

The Z-coordinate inversion aligns the coordinate system with radar conventions. To ground the pose, an offset is applied based on the lowest ankle joint:

$$\begin{aligned} z_{\text{offset}} &= \min(\mathbf{P}_z^{\text{rel}}(11), \mathbf{P}_z^{\text{rel}}(14)) \\ \mathbf{P}_z^{\text{grounded}} &= \mathbf{P}_z^{\text{rel}} - z_{\text{offset}} \end{aligned}. \quad (17)$$

The absolute position $\mathbf{Pos}_{\text{abs}} = (x_{\text{abs}}, y_{\text{abs}}, z_{\text{abs}})$ is updated frame-by-frame via pixel displacement of the hip center, scaled by α_{hum} , with $z_{\text{abs}} = 0$ initially, where $x_{\text{abs}}, y_{\text{abs}}, z_{\text{abs}}$ are the absolute coordinates. The final metric pose is:

$$\mathbf{P}_{\text{meters}} = [\mathbf{P}_x^{\text{rel}} + x_{\text{abs}}, \mathbf{P}_y^{\text{rel}} + y_{\text{abs}}, \mathbf{P}_z^{\text{grounded}} + z_{\text{abs}}]. \quad (18)$$

The resulted $\mathbf{P}_{\text{meters}}$ will be used for subsequent Kalman filtering-based temporal smoothing.

D. Temporal Smoothing for 3D Pose

To mitigate jitter, a Kalman filter is applied to each joint's 3D trajectory [44]. The temporal relationships between joints for prediction and constraint is used, resulting in smoother estimated 3D poses. Assume the state vector of the estimated 3D pose is:

$$\mathbf{st}_{\text{meters}} = [\mathbf{P}_{\text{meters}}, \dot{\mathbf{P}}_{\text{meters}}]^T, \quad (19)$$

with transition matrix:

$$\mathbf{TransP} = \begin{bmatrix} \mathbf{I}_{3 \times 3} & \Delta t_f \cdot \mathbf{I}_{3 \times 3} \\ \mathbf{0}_{3 \times 3} & \mathbf{I}_{3 \times 3} \end{bmatrix}. \quad (20)$$

The measurement matrix is $\mathbf{MeasP} = [\mathbf{I}_{3 \times 3}, \mathbf{0}_{3 \times 3}]$. Process and measurement noise covariances are set empirically. For each joint, prediction and correction steps yield a smoothed pose, enhancing stability during occlusions or detection losses.

The above pipeline enables accurate 3D kinematics for downstream radar simulation, bridging computer vision outputs with physics-based modeling.

III. RADAR MODULE

In this section, pose interpolation, filtering, and echo modeling in free-space and TTW scenarios with multipath effects are first introduced. Pulse compression and MTI are then employed to generate the RTM, while the STFT is used to generate the DTM. Next, the DnCNN model is utilized to perform denoising and micro-Doppler signature enhancement, and the ridge features on DTM are extracted using MLE.

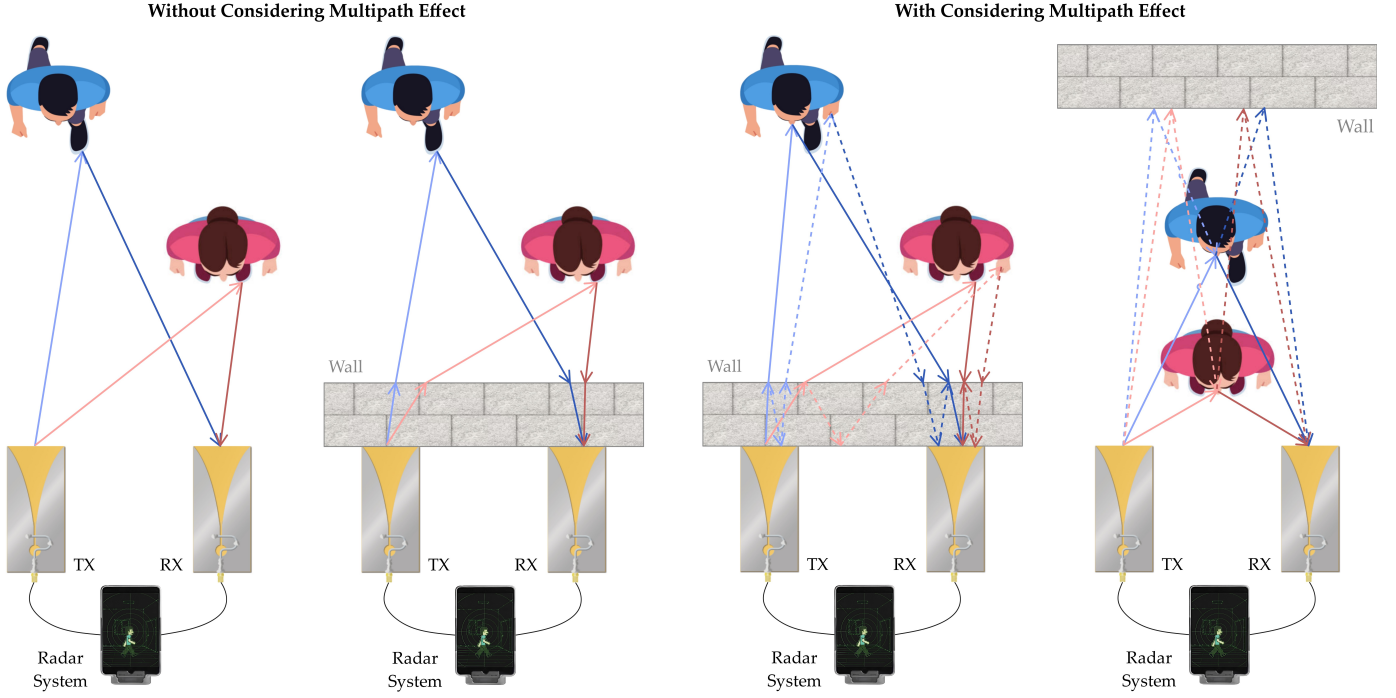


Fig. 7. Echo modeling of the radar simulation. Schematics from left to right represent: Free-space, TTW, TTW with multipath, free-space with multipath.

A. Pose Interpolation and Filtering

Assume the temporally smoothed 3D human pose is denoted as $\mathbf{P}_{j,p}$, where $p \in \mathbb{Z}^+ \cap [1, P]$ represents the p^{th} human target detected, and $j \in \mathbb{Z}^+ \cap [1, K_{\text{HRNet}}]$ represents the j^{th} joint. To convert the video timestamp t_f to the radar pulse t_m , linear interpolation is applied to the 3D pose results [45]:

$$\mathbf{P}'_{j,p}(t_m) = \mathbf{P}_{j,p}(t_f) + \frac{\mathbf{P}_{j,p}(t_f + \Delta t_f) - \mathbf{P}_{j,p}(t_f)}{\Delta t_f} (t_m - t_f) \quad (21)$$

$t_f \leq t_m < t_f + \Delta t_f$

The resulted 3D pose $\mathbf{P}'_{j,p}(t_m)$ is processed under Savitzky-Golay filtering to remove the noise and outliers. Let $\mathbf{x}_{\text{Sgolay}}$ represent a single coordinate's time series from $\mathbf{P}'_{j,p}$. For a point at time t_m , a window of $N_{\text{Sgolay}} = 2m + 1$ points is considered, indexed by a local variable $n \in \{-m, -m + 1, \dots, 0, \dots, m - 1, m\}$. The data points in this window are $\mathbf{x}_{\text{Sgolay}}(t_{m+n})$. A polynomial $p_{\text{Sgolay}}(n)$ is fitted to these points:

$$p_{\text{Sgolay}}(n) = \sum_{k=0}^{d_{\text{Sgolay}}} c_{\text{Sgolay},k} \cdot n^k, \quad (22)$$

where d_{Sgolay} is the order of Savitzky-Golay filtering [46], the coefficients $c_{\text{Sgolay},k}$ are found by minimizing the sum of squared errors E_{Sgolay} between the polynomial and the data:

$$\begin{aligned} E_{\text{Sgolay}} &= \sum_{n=-m}^m (p_{\text{Sgolay}}(n) - \mathbf{x}_{\text{Sgolay}}(t_{m+n}))^2 \\ &= \sum_{n=-m}^m \left(\left(\sum_{k=0}^{d_{\text{Sgolay}}} c_{\text{Sgolay},k} \cdot n^k \right) - \mathbf{x}_{\text{Sgolay}}(t_{m+n}) \right)^2. \end{aligned} \quad (23)$$

Solve the minimization problem of E_{Sgolay} using the least squares method to obtain the solution for $c_{\text{Sgolay},k}$. Substitute the smoothing polynomial p_{Sgolay} for $\mathbf{x}_{\text{Sgolay}}$ to reconstruct the twice-smoothed 3D pose matrix $\mathbf{P}''_{j,p}$, which serves as the input for the subsequent echo simulation.

B. Echo Modeling

The linear frequency-modulated (LFM) wave is used in this work [47]. The instantaneous frequency of LFM is defined as $f(t) = f_c + \mu t$, where f_c is the carrier frequency, μ is the frequency-modulated slope, t is the fast time. The phase of the signal is the integral of the angular frequency $\omega(t) = 2\pi f(t)$:

$$\theta_{\text{tx}}(t) = \int_0^t 2\pi(f_c + \mu\xi)d\xi = 2\pi \left(f_c t + \frac{1}{2}\mu t^2 \right). \quad (24)$$

The complex transmitted signal is therefore represented as:

$$s_{\text{tx}}(t) = \exp(j\theta_{\text{tx}}(t)) = \exp \left(j2\pi \left(f_c t + \frac{1}{2}\mu t^2 \right) \right). \quad (25)$$

The echo from a scatterer at a distance corresponding to a time delay τ is received as $s_{\text{rx}}(t) = A \cdot s_{\text{tx}}(t - \tau)$ with its phase representing as:

$$\begin{aligned} \theta_{\text{rx}}(t) &= 2\pi \left(f_c(t - \tau) + \frac{1}{2}\mu(t - \tau)^2 \right) \\ &= 2\pi \left(f_c t - f_c \tau + \frac{1}{2}\mu t^2 - \mu t \tau + \frac{1}{2}\mu \tau^2 \right). \end{aligned} \quad (26)$$

This received signal is mixed with the transmitted signal and low-pass filtered known as de-chirping-based pulse compression, which multiplies $s_{\text{rx}}(t)$ by the complex conjugate of $s_{\text{tx}}(t)$, which is $s_{\text{tx}}^*(t) = \exp(-j\theta_{\text{tx}}(t))$. The phase of the

resulting intermediate frequency (IF) signal is the difference between the received and transmitted phases:

$$\begin{aligned}\theta_{\text{if}}(t) &= \theta_{\text{rx}}(t) - \theta_{\text{tx}}(t) \\ &= 2\pi \left[\left(f_c t - f_c \tau + \frac{1}{2} \mu t^2 - \mu t \tau + \frac{1}{2} \mu \tau^2 \right) \right. \\ &\quad \left. - \left(f_c t + \frac{1}{2} \mu t^2 \right) \right] \\ \Rightarrow \theta_{\text{if}}(t) &= 2\pi \left(-f_c \tau - \mu t \tau + \frac{1}{2} \mu \tau^2 \right)\end{aligned}\quad (27)$$

By convention and noting that the sign of the frequency term depends on the specific de-chirping architecture, the phase is typically expressed to yield a positive beat frequency. The resulting complex baseband signal for a single scatterer is:

$$s_{\text{if}}(t, \tau) = A \cdot \exp \left(j2\pi \left(f_c \tau + \mu t \tau - \frac{1}{2} \mu \tau^2 \right) \right). \quad (28)$$

When a plane wave encounters a dielectric wall, its propagation is governed by the material's properties [48]. Starting from Maxwell's curl equations in a lossy medium, the Helmholtz wave equation is derived:

$$\nabla^2 \mathbf{E} - \gamma^2 \mathbf{E} = 0, \quad (29)$$

where γ is the complex propagation constant. For a medium with complex permittivity $\epsilon_c = \epsilon' - j\epsilon'' = \epsilon_r \epsilon_0 (1 - j \tan \delta)$, where $\tan \delta$ is the loss tangent, and permeability μ_0 , γ can be given by:

$$\gamma = \sqrt{j\omega\mu_0(\sigma + j\omega\epsilon')} = j\omega\sqrt{\mu_0\epsilon_c} = \alpha + j\beta, \quad (30)$$

where α is the attenuation constant and β is the phase constant. The intrinsic impedance of the wall η_{wall} is:

$$\eta_{\text{wall}} = \sqrt{\frac{j\omega\mu_0}{\sigma + j\omega\epsilon'}} = \sqrt{\frac{\mu_0}{\epsilon_c}}. \quad (31)$$

At an air-wall interface (Assuming from medium 1 to medium 2), boundary conditions require the tangential components of E^w and H^w to be continuous. For a normally incident wave, this leads to:

$$E_i^w + E_r^w = E_t^w, \quad H_i^w + H_r^w = H_t^w. \quad (32)$$

Using the relation $H^w = E^w/\eta$, where $\eta_1 = \eta_0$ as the impedance of air and $\eta_2 = \eta_{\text{wall}}$:

$$\frac{E_i^w}{\eta_1} - \frac{E_r^w}{\eta_1} = \frac{E_t^w}{\eta_2}. \quad (33)$$

Solving these two simultaneous equations for the reflection coefficient $\Gamma^w = E_r^w/E_i^w$ and transmission coefficient $T^w = E_t^w/E_i^w$ yields:

$$\begin{aligned}\Gamma_{12}^w &= \frac{\eta_2 - \eta_1}{\eta_2 + \eta_1} = \frac{\eta_{\text{wall}} - \eta_0}{\eta_{\text{wall}} + \eta_0} \\ T_{12}^w &= 1 + \Gamma_{12}^w = \frac{2\eta_2}{\eta_2 + \eta_1} = \frac{2\eta_{\text{wall}}}{\eta_{\text{wall}} + \eta_0}\end{aligned}\quad (34)$$

For the wall-air interface (Assuming from medium 2 to medium 1), the coefficients are $\Gamma_{21}^w = (\eta_1 - \eta_2)/(\eta_1 + \eta_2) = -\Gamma_{12}^w$ and $T_{21}^w = 1 + \Gamma_{21}^w$.

When the wall is present, multipath effects should also be considered. The total IF signal is the coherent sum of signals from all propagation paths [49]:

(1) Direct Transmission of Target Behind the Wall:

The signal passes TTW with thickness d_w , reflects off the target, and passes back TTW. The one-way complex transmission factor is the product of transmission at the first interface, propagation TTW, and transmission at the second interface: $T_{12}^w \cdot e^{-\gamma d_w} \cdot T_{21}^w$. The total two-way complex transmission factor T_{tw}^w is the square of the one-way factor:

$$T_{\text{tw}}^w = (T_{12}^w \cdot T_{21}^w \cdot e^{-\gamma d_w})^2. \quad (35)$$

The propagation time inside the wall is longer than in air. The phase velocity in the wall is $v_p = \frac{\omega}{\beta} = \frac{c}{n_{\text{wall}}}$, where $n_{\text{wall}} = \text{Re} \left\{ \sqrt{\frac{\epsilon_c}{\epsilon_0}} \right\}$ is the refractive index. The extra time delay for a one-way trip TTW is $\Delta t = \frac{d_w}{v_p} - \frac{d_w}{c} = \frac{d_w(n_{\text{wall}} - 1)}{c}$. For a two-way path, the total extra delay is $2\Delta t$. The effective time delay, τ' , is:

$$\tau'_{j,p}(t_m) = \frac{R_{j,p}(t_m)}{c} + \frac{2d_w(n_{\text{wall}} - 1)}{c}, \quad (36)$$

where $R_{j,p}(t_m)$ is the range of the p^{th} target and its j^{th} joint. The IF signal for this path is found by using τ' in Eq. (28) and scaling by T_{tw}^w .

(2) Internal Multipath of Target Behind the Wall:

A multipath component arises from internal reverberations. For a signal that bounces once inside the wall on each joint, the following paths should be considered: Enters wall (T_{12}^w), propagates to back face ($e^{-\gamma d_w}$) → Reflects from back face (Γ_{21}^w), propagates to front face ($e^{-\gamma d_w}$) → Reflects from front face (Γ_{21}^w), propagates to back face ($e^{-\gamma d_w}$) → Exits wall (T_{21}^w). Therefore, the one-way factor is $T_{12}^w \cdot \Gamma_{21}^w \cdot T_{21}^w \cdot e^{-3\gamma d_w}$. The two-way complex factor, $T_{\text{multipath}}$, is the square of this:

$$T_{\text{multipath}} = (T_{12}^w \cdot \Gamma_{21}^w \cdot T_{21}^w \cdot e^{-3\gamma d_w})^2. \quad (37)$$

This path travels an additional distance of $2d_w$ within the wall for each joint compared to the direct path. The effective two-way time delay τ'' is:

$$\tau''_{j,p}(t_m) = \tau'_{j,p}(t_m) + \frac{4d_w \cdot n_{\text{wall}}}{c}. \quad (38)$$

(3) Reflection Multipath of Target in Front of the Wall:

Using the method of images, where virtual transmitter \mathbf{P}'_{tx} and receiver \mathbf{P}'_{rx} are reflections of the true antennas across the wall face, the multipath path lengths are calculated geometrically. The corresponding echoes are scaled by the reflection coefficient Γ_{12}^w for each bounce off the wall. The time delays (τ_a, τ_b, τ_c) for the three primary multipath components are:

$$\begin{aligned}\tau_a &= \frac{\|\mathbf{P}''_{j,p} - \mathbf{P}'_{\text{tx}}\| + \|\mathbf{P}''_{j,p} - \mathbf{P}'_{\text{rx}}\|}{c} \\ \tau_b &= \frac{\|\mathbf{P}''_{j,p} - \mathbf{P}'_{\text{tx}}\| + \|\mathbf{P}''_{j,p} - \mathbf{P}'_{\text{rx}}\|}{c} \\ \tau_c &= \frac{\|\mathbf{P}''_{j,p} - \mathbf{P}'_{\text{tx}}\| + \|\mathbf{P}''_{j,p} - \mathbf{P}'_{\text{rx}}\|}{c}\end{aligned}\quad (39)$$

The final IF signal, $S_{\text{if}}(t, t_m)$, is the coherent sum of the primary path and all applicable multipath components, plus

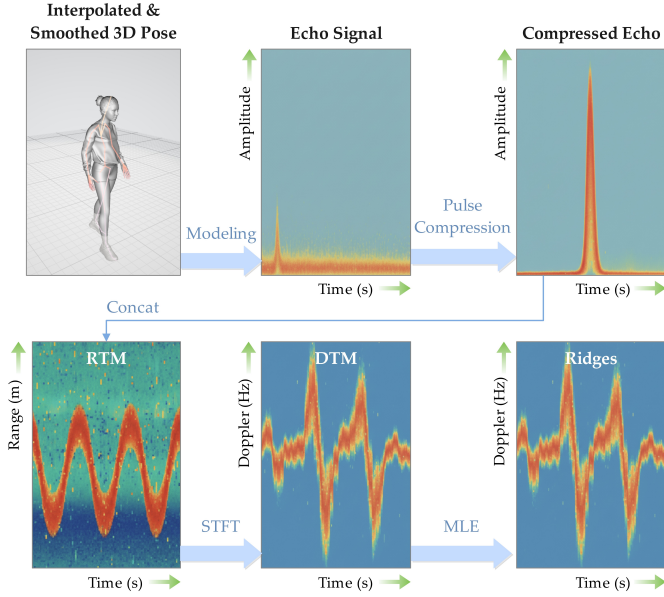


Fig. 8. The flowchart of generating R/DTM with ridge extraction.

complex white Gaussian noise $\mathbf{n}(t)$.

C. RTM and DTM Generation

As shown in Fig. 8, the RTM is generated by applying the fast Fourier transform (FFT) along the fast-time axis of the total IF signal for each pulse [50]:

$$\text{RTM}(r, t_m) = |\mathcal{F}\{S_{\text{if}}(t, t_m)\}|, \quad (40)$$

where r is the range bin of the RTM. A two-pulse canceller is applied to the complex range profiles to suppress static clutter:

$$\text{RTM}_{\text{MTI}}(r, t_m) = |\mathcal{F}\{S_{\text{if}}(t, t_m)\} - \mathcal{F}\{S_{\text{if}}(t, t_{m-1})\}|. \quad (41)$$

The DnCNN model is proposed for noise suppression and micro-Doppler signature enhancement on MTI-processed RTM [51]. The DnCNN model takes the noisy map as input, preprocessing them using a 3×3 convolutional layer with 64 channels and a rectified linear unit (ReLU) activation function. The model then stacks bottlenecks consisting of 18 repetitions of 3×3 convolutions, batch normalization, and ReLU activation functions in sequence. Finally, a 3×3 convolution with a channel count of 1 is used to estimate the noise mask map. Subtract the input image from the noise mask to obtain a map that is denoised and feature-enhanced.

The primary objective of the loss function of DnCNN model is to minimize the mean squared error between the residual map output by the network and the true label map, expressed as:

$$\mathcal{L}_{\text{DnCNN}}(\theta_{\text{DnCNN}}) = \frac{\|Q(y_{\text{DnCNN},i}; \theta_{\text{DnCNN}}) - (y_{\text{DnCNN},i} - x_{\text{DnCNN},i})\|^2}{2N_{\text{DnCNN}}}, \quad (42)$$

where $y_{\text{DnCNN},i}$ is the noisy input map, $x_{\text{DnCNN},i}$ is the true label map, $Q(y_{\text{DnCNN},i})$ is the inference output of the DnCNN, N_{DnCNN} is the number of training batch, and θ_{DnCNN} is the parameter of the DnCNN model. Thus, it is important to note that the input to the DnCNN must be a map with absolute values.

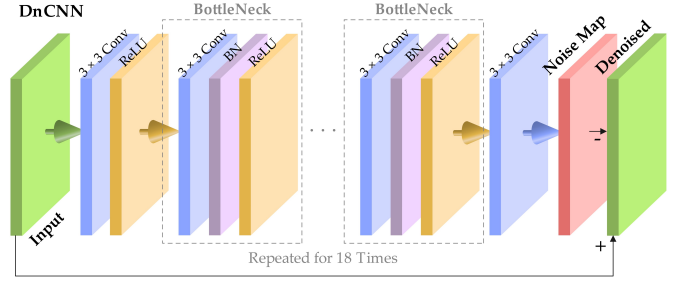


Fig. 9. Structure design of the DnCNN model.

Furthermore, the input for subsequent DTM generation must be the MTI-processed RTM prior to DnCNN enhancement.

The DTM is generated via the STFT of a slow-time signal, which is derived from the range summation of the MTI-processed RTM:

$$\text{DTM}(f_d, \tau) = \left| \int_{-\infty}^{\infty} \sum_r (\text{RTM}_{\text{MTI}}(r, t_m)) \cdot \text{win}(t_m - \tau) e^{-j2\pi f_d t_m} dt_m \right|, \quad (43)$$

where f_d is the Doppler axis of DTM, and $\text{win}(\cdot)$ is the window function of STFT, with the preset window length and overlap ratio. DTM can also undergo denoising and micro-Doppler signature enhancement via DnCNN.

D. Ridge Feature Extraction

The most prominent micro-Doppler signature is extracted from the DTM by identifying the N_r time-frequency ridges [52], $\{f_{\text{ridge},k}(\tau) \mid k = 1, \dots, N_r\}$, corresponding to the paths of MLE. This is achieved by finding the N_r largest local maxima of $\text{DTM}(f_d, \tau)$ for each time instant τ and connecting them through time:

$$\{f_{\text{ridge},k}(\tau)\}_{k=1}^{N_r} = \arg \max_{f_d} \{\text{DTM}(f_d, \tau)\}_{N_r}. \quad (44)$$

The generated DTM images, the sequence of extracted time-frequency ridges, or the curve images plotted from time-frequency ridges can all be fed into neural network models to achieve HAR [53].

IV. HYBRID PARALLEL-SERIAL NEURAL NETWORK MODEL FOR RADAR-BASED HAR

As shown in Fig. 10, in this paper, the SPNet is proposed as an example for achieving the mapping from R/DTM to activity labels [54]. The input data of SPNet represented as a multi-dimensional tensor is first fed into an initial convolutional block consisting of a 3×3 convolution layer followed by batch normalization (BN). This is succeeded by a series of densely connected convolutional layers, where each subsequent 3×3 convolution layer receives concatenated feature maps from all preceding layers for promoting feature reuse. A 1×1 convolution is applied after concatenation to reduce dimensionality and fuse features efficiently. Following the dense block, an adding operation is performed to merge residual connections, and this structure is repeated three times to form a multi-stage feature extraction pipeline. In each repetition,

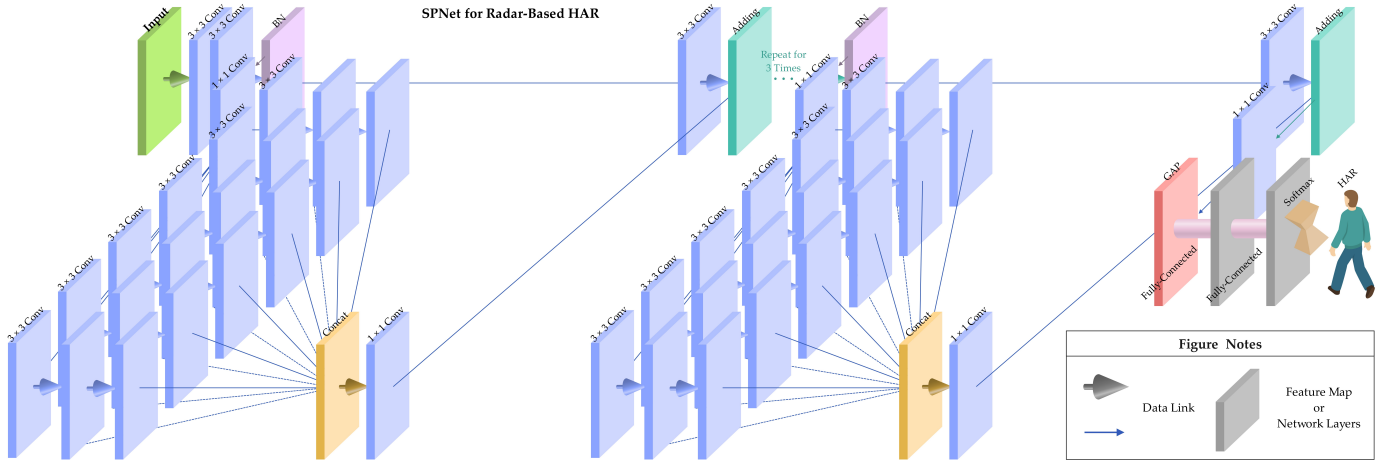


Fig. 10. Structure for the designed SPNet used for radar-based HAR task.

TABLE I
EXPERIMENTAL PARAMETER SETTINGS.

| Parameter | Free-Space | Through-the-Wall |
|------------------------------|------------|------------------|
| Radar Parameters | | |
| Carrier Frequency | 77 GHz | 2 GHz |
| Bandwidth | 4 GHz | 1 GHz |
| Pulse Repetition Frequency | 8192 Hz | 128 Hz |
| Sampling Frequency | | 10 MHz |
| Pulse Duration | | 40 μ s |
| Transmitter Position | | (-0.1, 0, 1.5) m |
| Receiver Position | | (0.1, 0, 1.5) m |
| Antenna Gain | | 10 dBi |
| Antenna Isolation | | 20 dB |
| SNR | | 50 dB |
| Wall Parameters | | |
| Wall Center Position | / | (-0.1, 0, 1.5) m |
| Wall Dimensions | / | (5, 0.24, 2.5) m |
| Relative Dielectric Constant | / | 6 |
| Loss Tangent | / | 0.03 |

TABLE II
UNIFORM HYPERPARAMETERS FOR NETWORKS.

| Name of Hyperparameters | Value |
|-------------------------------------|--------------------|
| Batch Size | 64 |
| Total Epoches | 20 |
| Initial Learning Rate ¹ | 0.00147 |
| Regularization Method | $L - 2$ |
| Optimizer | Adam |
| Solidified Model | Best Epoch |
| Training Dataset | 2880 |
| Validation Dataset | 720 |
| Hardware of Training and Validation | NVIDIA RTX 3060 OC |
| Software of Training and Validation | Matlab R2025b |

additional 3×3 convolution layers with batch normalization are incorporated, and 1×1 convolutions are utilized for channel adjustment. The output from these repeated blocks is then directed to a final convolutional stage, which includes further 3×3 convolutions and concatenation, leading to a global average pooling (GAP) layer that aggregates spatial features into a compact representation. The pooled features are subsequently passed through a fully-connected layer to

produce class logits, after which a softmax activation is applied to generate probability distributions for HAR categories.

The cross-entropy loss function for the network is designed to measure the discrepancy between predicted probabilities and true activity labels in a multi-class classification setting. Categorical cross-entropy is employed for SPNet, where the loss for a single sample is calculated as the negative sum of the true label distribution multiplied by the logarithm of the predicted probabilities:

$$\mathcal{L}_{\text{SPNet}} = - \sum_{i=1}^{\text{Cls}} y_{\text{SPNet},i} \log(p_{\text{SPNet},i}), \quad (45)$$

where Cls represents the number of classes, $y_{\text{SPNet},i}$ denotes the one-hot encoded true label for class i , and $p_{\text{SPNet},i}$ signifies the predicted probability for class i . This loss is averaged over all samples in a batch during training to optimize the network parameters. Network models can be trained separately using RTM, DTM, channel-merged R/DTM, or DTM ridge images. New input data can be fed into the network for inference to obtain HAR results.

V. NUMERICAL EXPERIMENTS

A thorough validation of the data produced by the constructed simulator, including visualizations, comparative verifications, ablation experiments, and the suggested neural network's performance is provided and discussed detailedly in this section.

A. Experimental Settings

The parameters of the kinematic model and the radar echo model can be changed in the simulator, as indicated in TABLE I. Free-space detection [55] and TTW detection [56] are the two scenarios used for analysis in this paper.

In free-space detection scenario, the radar's carrier frequency is set to 77 GHz with a bandwidth of 4 GHz. A PRF of 8192 Hz and a sampling frequency of 10 MHz are used, with a pulse duration of 40 μ s. The transmitter and receiver are positioned at (-0.1, 0, 1.5) m and (0.1, 0, 1.5) m, respectively. An antenna gain of 10 dBi and an antenna isolation of 20 dB

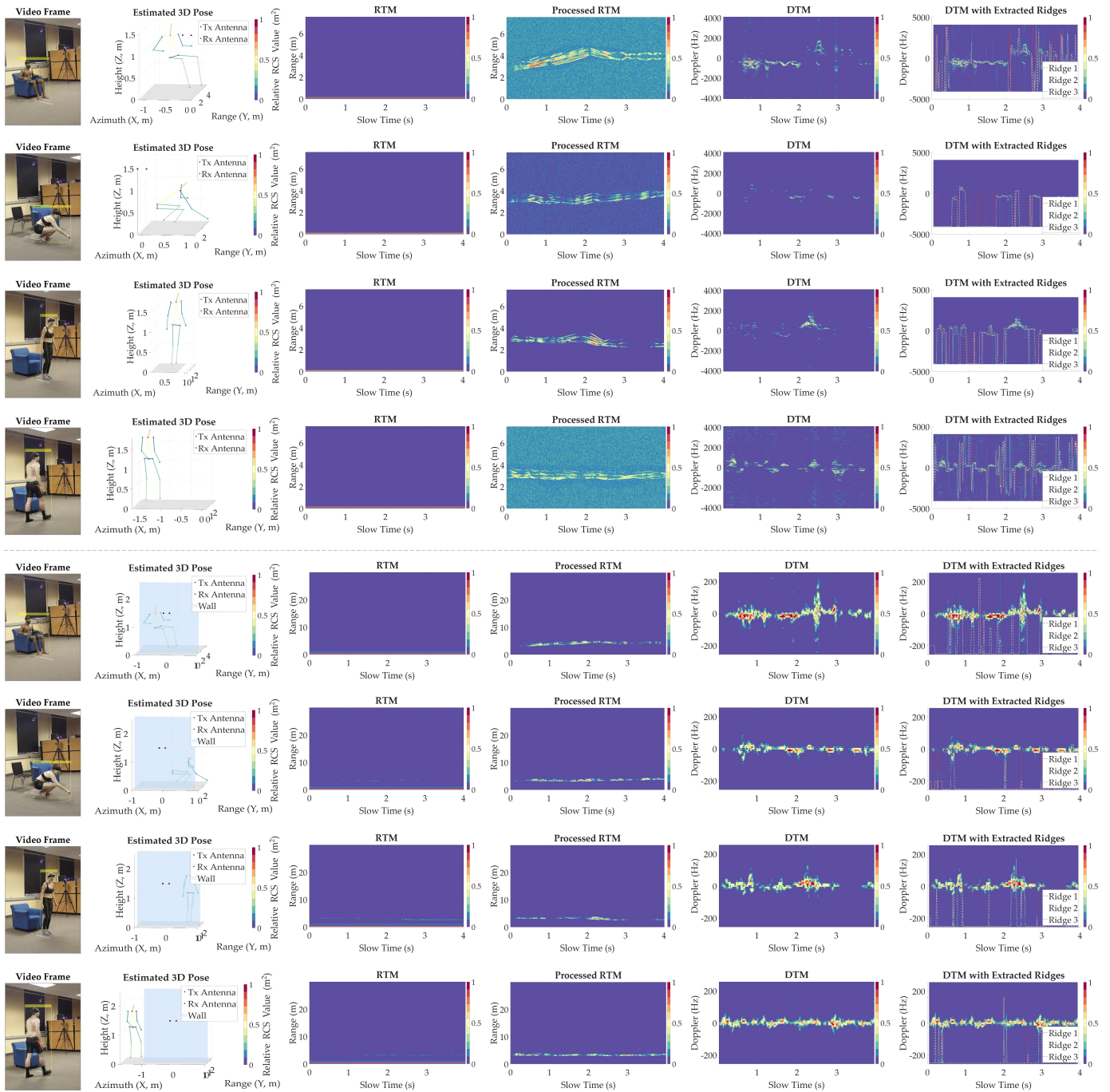


Fig. 11. Visualizations under OSSet: The first row is for free-space sitting down activity, the second row is for grabbing, the third row is for standing up, the forth row is for walking, and row 5 to row 8 follow the same activities as the first four rows, with the simulation scenario being shifted to TTW.

are specified, and a signal-to-noise ratio (SNR) of 50 dB is assumed.

In TTW detection scenario, the radar's carrier frequency is changed to 2 GHz with a bandwidth of 1 GHz. A pulse repetition frequency of 128 Hz is used. The center of the wall is placed at $(-0.1, 0, 1.5)$ m. The length, width, and height of the wall are 0.24, 5, and 2.5 m, respectively. The relative dielectric constant and the loss tangent of the wall are 6 and 0.03, respectively. The rest of the parameters remain the same as free-space detection.

For experimental human activities, there are 12 categories

designed for the network training and inference labels, including: Empty (S1), Punching (S2), Kicking (S3), Grabbing (S4), Sitting Down (S5), Standing Up (S6), Rotating (S7), Walking (S8), Sitting to Walking (S9), Walking to Sitting (S10), Falling to Walking (S11), and Walking to Falling (S12) [33]. Two datasets are constructed using open-source data (OSSet) and our own recorded data (RWSet), each containing 300 groups per class. The data is randomly cut in 8 : 2 ratio for training and validation. The OSSet is compiled by searching and curating multiple free works within the field [57]–[61]. Both OSSet and RWSet are divided into groups of

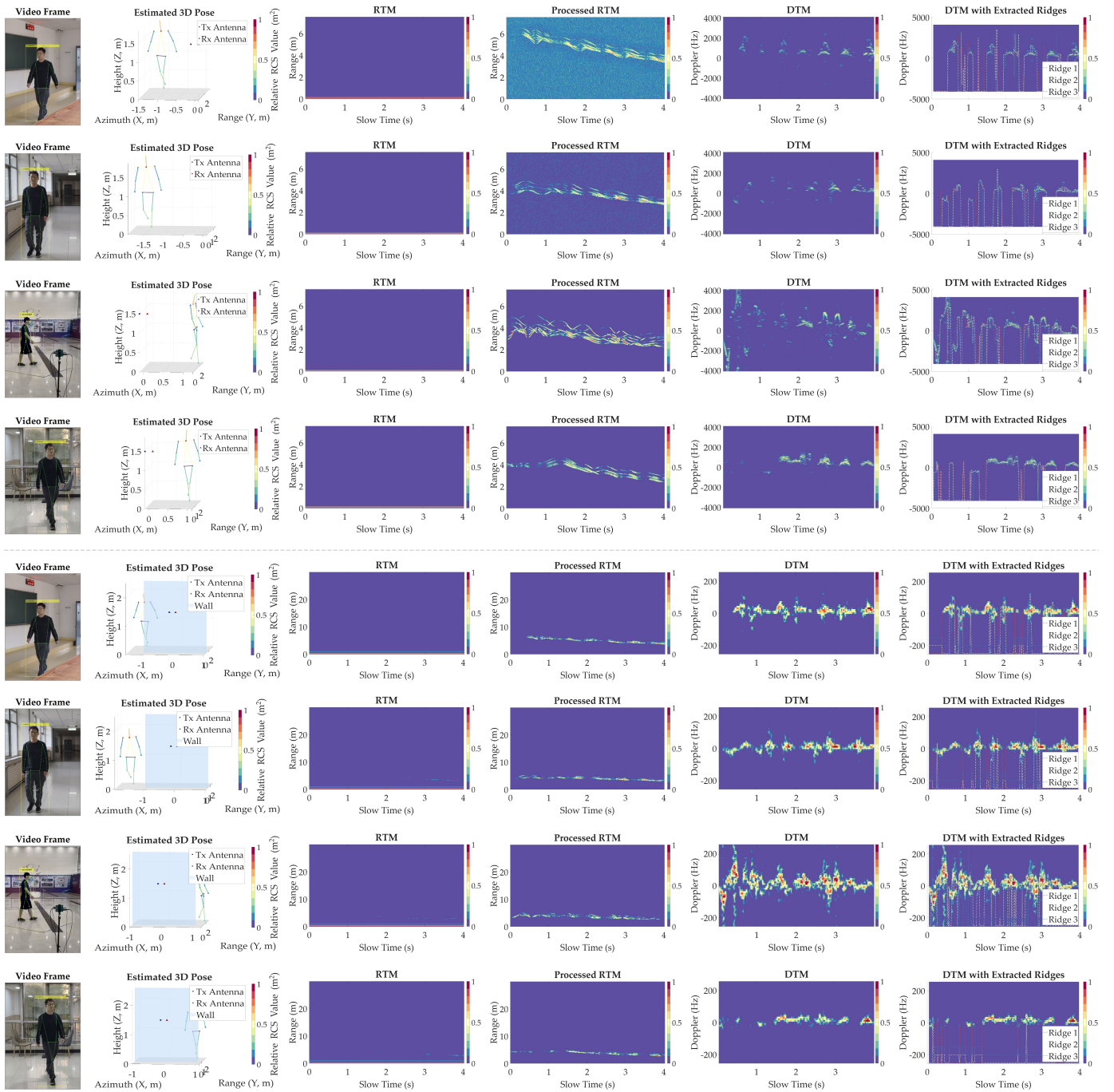


Fig. 12. Visualizations using RWSet: Row 1 to 4 are used for free-space simulation taken from classroom, corridor, hall, and pantry, respectively, and row 5 to row 8 change the simulation scenario to TTW.

approximately 4 seconds each. In addition, the hyperparameter settings for network training are shown in TABLE II.

B. Visualizations

As shown in Fig. 11 and 12, the data generated by the computer vision module and the radar module proposed in the paper are both visualized. Experiments are conducted in Fig. 11 using open-source HAR video dataset, where the estimated 3D pose, RTM, processed RTM, DTM, and ridge feature extraction results under several typical activities are

compared. Fig. 12 presents the visualization of data recorded by ourselves.

From Fig. 11, it can be seen that the estimated 3D poses are close to the real videos in terms of structure and spatial position. The generated RTM and DTM can reflect key information about the motion of human joints. Except for the DTM features that are disconnected in the images, effective time-frequency ridges can all be extracted. The motion trends of human joints in free-space and TTW scenarios are consistent with the video trends. Similar conclusions can be drawn from Fig. 12, and the quality of the generated data is not affected

TABLE III
PSNR COMPARISON BETWEEN MAPS GENERATED BY OSSet AND FROM ACTUAL MEASUREMENTS UNDER IDENTICAL RADAR SETTINGS*.

| Name of the Maps | OSSet (dB) | | | | | | | | | | | | Average among Activities ¹ |
|----------------------------|------------|-------|-------|-------|-------|-------|-------|-------|-------|-------|-------|-------|---------------------------------------|
| | S1 | S2 | S3 | S4 | S5 | S6 | S7 | S8 | S9 | S10 | S11 | S12 | |
| Free-Space Scenario | | | | | | | | | | | | | |
| RTM | 42.15 | 38.72 | 45.33 | 36.91 | 43.88 | 35.29 | 40.17 | 44.64 | 39.52 | 41.06 | 37.84 | 45.91 | 40.95 |
| Processed RTM | 18.52 | 24.11 | 15.79 | 22.68 | 13.94 | 25.33 | 19.86 | 16.47 | 23.05 | 14.71 | 21.22 | 17.98 | 19.47 |
| DTM | 20.31 | 25.88 | 17.65 | 24.03 | 15.21 | 25.92 | 21.49 | 18.01 | 24.76 | 16.35 | 23.17 | 19.55 | 21.03 |
| TTW Scenario | | | | | | | | | | | | | |
| RTM | 40.26 | 37.81 | 44.19 | 35.88 | 42.05 | 36.74 | 39.92 | 45.81 | 38.14 | 43.57 | 36.23 | 44.99 | 40.47 |
| Processed RTM | 16.73 | 22.48 | 14.99 | 20.15 | 13.24 | 24.81 | 17.36 | 15.91 | 21.77 | 14.02 | 19.64 | 16.03 | 17.76 |
| DTM | 18.11 | 23.97 | 16.25 | 22.84 | 14.78 | 25.13 | 19.02 | 17.56 | 23.31 | 15.89 | 21.08 | 18.42 | 19.70 |

* This experiment compared the PSNR of maps generated by OSSet with that of real-world maps under identical radar settings and activity categories. All results represent the average of 10 randomly selected datasets.

¹ Take the average of the PSNR results for all 12 activities.

TABLE IV
PSNR COMPARISON BETWEEN MAPS GENERATED BY RWSet AND FROM ACTUAL MEASUREMENTS UNDER IDENTICAL RADAR SETTINGS*.

| Name of the Maps | RWSet (dB) | | | | | | | | | | | | Average among Activities ¹ |
|----------------------------|------------|-------|-------|-------|-------|-------|-------|-------|-------|-------|-------|-------|---------------------------------------|
| | S1 | S2 | S3 | S4 | S5 | S6 | S7 | S8 | S9 | S10 | S11 | S12 | |
| Free-Space Scenario | | | | | | | | | | | | | |
| RTM | 43.52 | 48.19 | 41.76 | 46.93 | 49.21 | 40.88 | 45.34 | 42.67 | 47.88 | 44.15 | 40.23 | 46.56 | 44.78 |
| Processed RTM | 28.14 | 32.77 | 24.59 | 35.01 | 37.82 | 21.93 | 29.66 | 31.04 | 23.48 | 36.15 | 26.79 | 30.58 | 29.83 |
| DTM | 30.25 | 35.81 | 27.46 | 36.99 | 37.15 | 22.58 | 31.73 | 33.42 | 25.03 | 37.89 | 28.11 | 32.96 | 31.62 |
| TTW Scenario | | | | | | | | | | | | | |
| RTM | 41.82 | 46.25 | 40.19 | 44.76 | 48.91 | 41.33 | 47.02 | 43.18 | 45.97 | 48.05 | 42.64 | 47.41 | 44.79 |
| Processed RTM | 22.94 | 28.63 | 21.47 | 27.55 | 31.89 | 24.16 | 30.01 | 26.72 | 29.38 | 33.40 | 25.80 | 31.12 | 27.76 |
| DTM | 25.33 | 30.17 | 23.82 | 29.41 | 34.08 | 26.79 | 32.55 | 28.16 | 31.90 | 35.74 | 27.20 | 33.68 | 29.90 |

* This experiment compared the PSNR of maps generated by RWSet with that of real-world maps under identical radar settings and activity categories. All results represent the average of 10 randomly selected datasets.

¹ Take the average of the PSNR results for all 12 activities.

by common video recording scenarios. The above conclusions together provide qualitative proof of the effectiveness of the generated data.

C. Comparative Verification

The similarity between simulator-generated spectra and experimental data [36], [37] is first compared. Both the same activity categories and radar parameter settings are employed as the generated data. Peak signal-to-noise ratio (PSNR) is used to measure similarity between maps [62]. Assume that \mathbf{I}^{set} is the generated map, \mathbf{I}^{real} is the corresponding experimental map, and $\text{Max}_{\mathbf{I}^{\text{set}}}$ is the maximum pixel of \mathbf{I}^{set} . Then:

$$\text{PSNR} = 10 \cdot \log_{10} \left(\frac{H \cdot W \cdot \text{Max}_{\mathbf{I}^{\text{set}}}^2}{\sum_{i=0}^{H-1} \sum_{j=0}^{W-1} [\mathbf{I}^{\text{set}}_{i,j} - \mathbf{I}^{\text{real}}_{i,j}]^2} \right), \quad (46)$$

where H, W are the height and width of the map, respectively. Generally, PSNR values between 15 ~ 30 dB are considered similar, values between 30 ~ 40 dB are considered good similarity, and values between 40 ~ 50 dB are considered nearly identical.

In TABLE III and IV, the similarity between three kinds of spectra generated by the simulator and the measured spectra is compared across 12 different activities. From TABLE III, since the primary components in the RTM are the direct wave and the low-rank main echo from the wall, the similarity between the simulator and the measured spectrum is relatively high. The processed RTM and DTM primarily reflect the macro and

TABLE V
ABLATION EXPERIMENT OF THE TARGET DETECTION MODEL*.

| Methods | Maps | OSSet Average ¹ | RWSet Average ¹ |
|-----------------------------|---------------|----------------------------|----------------------------|
| Free-Space Scenario | | | |
| ACF + GNN ² | RTM | 39.12 | 42.63 |
| | Processed RTM | 17.92 | 27.42 |
| | DTM | 19.75 | 28.85 |
| RTMDet + MOSSE ³ | RTM | 39.83 | 42.83 |
| | Processed RTM | 18.42 | 27.82 |
| | DTM | 20.08 | 29.51 |
| Proposed Method | RTM | 40.95 | 44.78 |
| | Processed RTM | 19.47 | 29.83 |
| | DTM | 21.03 | 31.62 |
| TTW Scenario | | | |
| ACF + GNN | RTM | 37.92 | 41.65 |
| | Processed RTM | 15.78 | 24.87 |
| | DTM | 17.89 | 26.87 |
| RTMDet + MOSSE | RTM | 39.02 | 42.45 |
| | Processed RTM | 16.48 | 25.57 |
| | DTM | 18.39 | 27.37 |
| Proposed Method | RTM | 40.47 | 44.79 |
| | Processed RTM | 17.76 | 27.76 |
| | DTM | 19.70 | 29.90 |

* Existing human target detection works are referenced from [63]. To ensure the rigor of the experiment, the designs of other modules remain unchanged.

¹ Take the average of the PSNR results for all 12 activities in dB unit.

² ACF is the abbreviation of aggregate channel feature detector.

³ MOSSE is the abbreviation of minimum output sum of squared error correlation filtering tracking method.

micro-level characteristics of human joint motions, resulting in relatively low similarity. However, based on the average values of the 12 activities, the generated data remains valid. Similar conclusions can be drawn from TABLE IV. Since

TABLE VI
ABLATION EXPERIMENT OF THE POSE ESTIMATION MODEL*.

| Methods | Maps | OSSet Average ¹ | RWSet Average ¹ |
|-----------------------------|---------------|----------------------------|----------------------------|
| Free-Space Scenario | | | |
| CPM + Matching ² | RTM | 38.52 | 42.17 |
| | Processed RTM | 17.41 | 27.15 |
| | DTM | 18.93 | 28.56 |
| TCN ³ | RTM | 39.78 | 43.51 |
| | Processed RTM | 18.65 | 28.77 |
| | DTM | 20.14 | 30.29 |
| Proposed Method | RTM | 40.95 | 44.78 |
| | Processed RTM | 19.47 | 29.83 |
| | DTM | 21.03 | 31.62 |
| TTW Scenario | | | |
| CPM + Matching | RTM | 37.68 | 41.92 |
| | Processed RTM | 15.23 | 24.79 |
| | DTM | 16.94 | 26.33 |
| TCN | RTM | 39.15 | 43.08 |
| | Processed RTM | 16.59 | 26.13 |
| | DTM | 18.21 | 27.85 |
| Proposed Method | RTM | 40.47 | 44.79 |
| | Processed RTM | 17.76 | 27.76 |
| | DTM | 19.70 | 29.90 |

* Existing human pose estimation works are referenced from [64]. To ensure the rigor of the experiment, the designs of other modules remain unchanged.

¹ Take the average of the PSNR results for all 12 activities in dB unit.

² CPM is the abbreviation of convolutional pose machine.

³ TCN is the abbreviation of temporal convolutional network model.

RWSet aligns with the scenarios and activities observed in our measured radar spectrum, the similarity calculation results are significantly improved. Overall, the results above demonstrate the validity and effectiveness of the generated data.

D. Ablation Experiments

The human target detection and tracking method, the 3D pose estimation and temporal smoothing method, the radar echo modeling method, and the R/DTM feature enhancing method proposed in this paper are compared to existing methods in this paper as ablation experiments. aiming to prove the rationality of the structure design of the whole simulator. All ablations are conducted using similar methodology to TABLE III and IV, with PSNR metrics employed for comparison.

As shown in TABLE V, the proposed RTMDet and GNN-based design is compared to the existing human target detection and tracking methods [63]. The designs of other modules remain unchanged. The results indicate that modifying the human target detection method to the machine learning-based aggregate channel feature detector (ACF) approach leads to a decline in generated data quality due to reduced accuracy in bounding box positioning. Similarly, switching the tracking method to the minimum output sum of squared error (MOSSE) algorithm within the correlation filter causes tracking interruptions that degrade generated data quality. The conclusions obtained from simulations of free-space and TTW scenarios are consistent, which means that the design of the target detection method is reasonable.

As shown in TABLE VI, the proposed HRNet, nearest matching, and Kalman filtering-based design is compared to the existing human pose estimation methods [64]. The designs of other modules remain unchanged. Replacing the 2D pose estimation method with a convolutional pose machine (CPM) results in a decline in generated data quality. This

TABLE VII
ABLATION EXPERIMENT OF THE RADAR ECHO MODELING*.

| Methods | Maps | OSSet Average ¹ | RWSet Average ¹ |
|-----------------------------------|---------------|----------------------------|----------------------------|
| Free-Space Scenario | | | |
| w/o Wall Attenuation ² | RTM | 40.95 | 44.78 |
| | Processed RTM | 19.47 | 29.83 |
| | DTM | 21.03 | 31.62 |
| w/o Multipath Effect | RTM | 40.95 | 44.78 |
| | Processed RTM | 19.47 | 29.83 |
| | DTM | 21.03 | 31.62 |
| Proposed Method | RTM | 40.95 | 44.78 |
| | Processed RTM | 19.47 | 29.83 |
| | DTM | 21.03 | 31.62 |
| TTW Scenario | | | |
| w/o Wall Attenuation | RTM | 34.67 | 38.41 |
| | Processed RTM | 13.56 | 22.03 |
| | DTM | 14.82 | 23.49 |
| w/o Multipath Effect | RTM | 38.47 | 42.15 |
| | Processed RTM | 16.03 | 25.54 |
| | DTM | 17.75 | 27.32 |
| Proposed Method | RTM | 40.47 | 44.79 |
| | Processed RTM | 17.76 | 27.76 |
| | DTM | 19.70 | 29.90 |

* To ensure the rigor of the experiment, the designs of other modules remain unchanged.

¹ Take the average of the PSNR results for all 12 activities in dB unit.

² w/o is the abbreviation of word "without".

TABLE VIII
ABLATION EXPERIMENT OF THE FEATURE ENHANCING MODEL*.

| Methods | Maps | OSSet Average ¹ | RWSet Average ¹ |
|----------------------------|---------------|----------------------------|----------------------------|
| Free-Space Scenario | | | |
| Perona-Malik ² | RTM | 40.81 | 44.62 |
| | Processed RTM | 17.55 | 27.91 |
| | DTM | 19.24 | 29.75 |
| KSVD ³ | RTM | 40.73 | 44.59 |
| | Processed RTM | 18.12 | 28.34 |
| | DTM | 19.86 | 30.11 |
| Proposed Method | RTM | 40.95 | 44.78 |
| | Processed RTM | 19.47 | 29.83 |
| | DTM | 21.03 | 31.62 |
| TTW Scenario | | | |
| Perona-Malik | RTM | 40.31 | 44.61 |
| | Processed RTM | 15.82 | 25.88 |
| | DTM | 17.53 | 27.64 |
| KSVD | RTM | 40.25 | 44.52 |
| | Processed RTM | 16.49 | 26.21 |
| | DTM | 18.06 | 28.03 |
| Proposed Method | RTM | 40.47 | 44.79 |
| | Processed RTM | 17.76 | 27.76 |
| | DTM | 19.70 | 29.90 |

* Existing image-based feature enhancing and denoising models are referenced from [65]. To ensure the rigor of the experiment, the designs of other modules remain unchanged.

¹ Take the average of the PSNR results for all 12 activities in dB unit.

² Classic anisotropic diffusion filtering methods.

³ KSVD is the abbreviation of K-singular value decomposition.

occurs because the CPM lacks the powerful multi-scale high-resolution feature representation capabilities of an HRNet, leading to positional shifts in the detected joints. TCN also possesses temporal modeling capabilities, but the absolute 3D positions it estimates for human targets are imprecise, which can also lead to a decline in generated data quality. The conclusions obtained from simulations of free-space and TTW scenarios are consistent, which means that the design of the pose estimation method is reasonable.

As shown in TABLE VII, the proposed radar echo modeling

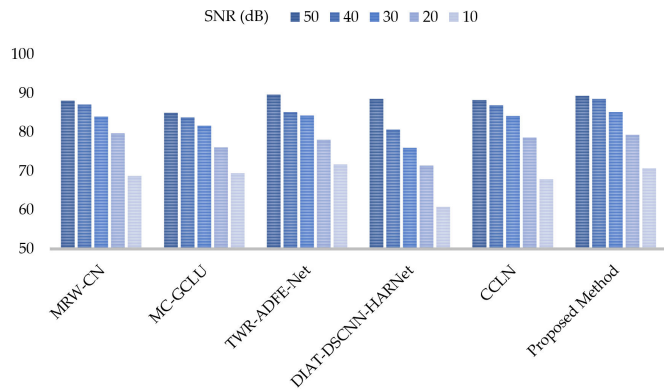


Fig. 15. Robustness testing using OSSet.

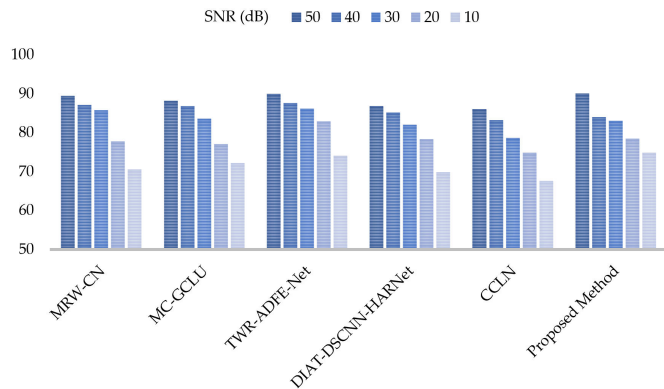


Fig. 16. Robustness testing using RWSet.

and location estimation methods can be adopted. Additionally, more lightweight models can be designed to improve inference speed.

(2) Feature Extraction Issues: Although ridge features extracted using MLE demonstrate certain effectiveness, experimental results indicate that these features fail when micro-Doppler signature on the simulated maps is discontinuous. More robust feature extraction methods require consideration.

(3) Network Physical Interpretability Issues: The designed SPNet method for radar-based HAR is effective. However, when the training data input to the network is changed from image-based DTM to ridge feature, employing a better temporal sequence modeling neural network model or a graph-based neural network model yields superior physical interpretability. This theoretically results in improved accuracy and robustness.

VI. CONCLUSION

To solve the problem that a comprehensive simulation method for radar-based HAR has still not been developed in this field, and existing software has been developed based on models or motion-captured data, resulting in limited flexibility, RadHARSimulator V2 has been presented in this paper. Both computer vision and radar modules have been included in the simulator. In the computer vision module, the RTMDet with GNN has first been used to detect and track human targets in the video. Then, the HRNet has been used to estimate 2D poses of the detected human targets. Next, the 3D poses

of the detected human targets have been obtained by the nearest matching method. Finally, smooth temporal 3D pose estimation has been achieved through Kalman filtering. In the radar module, pose interpolation and smoothing have first been achieved through the Savitzky-Golay method. Second, the delay model and the mirror method have been used to simulate echoes in both free-space and TTW scenarios. Then, the RTM has been generated using pulse compression, MTI, and DnCNN. Next, the DTM has been generated using STFT and DnCNN again. Finally, the ridge features on the DTM have been extracted using the MLE method. In addition, a SPNet architecture has been proposed for radar-based HAR. Numerical experiments have been conducted and analyzed to demonstrate the effectiveness of the designed simulator and the proposed network model.

VII. ACKNOWLEDGEMENT

This is the upgraded version of my previous work [RadHAR-Simulator V1](#). Our simulator is inspired by this interesting work [72]. We extend our sincere thanks for this.

I would also like to thank my mentors for the platform they have provided me.

My software has not undergone extensive testing by a large number of users. There may still be areas for improvement during use. I welcome your valuable feedback and would be very grateful!

REFERENCES

- [1] B. Erol and M. G. Amin, "Radar Data Cube Processing for Human Activity Recognition Using Multisubspace Learning," *IEEE Trans. Aerosp. Electron. Syst.*, vol. 55, no. 6, pp. 3617-3628, Dec. 2019.
- [2] X. Qiao, M. G. Amin, T. Shan, Z. Zeng and R. Tao, "Human Activity Classification Based on Micro-Doppler Signatures Separation," *IEEE Trans. Geosci. Remote Sens.*, vol. 60, pp. 1-14, 2022.
- [3] V. C. Chen, "Detection and analysis of human motion by radar," in *Proc. IEEE Radar Conf.*, Rome, Italy, pp. 1-4, 2008.
- [4] F. Cai, A. Patharkar, T. Wu, F. Y. M. Lure, H. Chen and V. C. Chen, "STRIDE: Systematic Radar Intelligence Analysis for ADRD Risk Evaluation With Gait Signature Simulation and Deep Learning," *IEEE Sensors J.*, vol. 23, no. 10, pp. 10998-11006, May. 2023.
- [5] A. Shrestha, H. Li, J. Le Kernec and F. Fioranelli, "Continuous Human Activity Classification From FMCW Radar With Bi-LSTM Networks," *IEEE Sensors J.*, vol. 20, no. 22, pp. 13607-13619, Nov. 2020.
- [6] H. Li, G. Cui, S. Guo, L. Kong and X. Yang, "Human Target Detection Based on FCN for Through-the-Wall Radar Imaging," *IEEE Geosci. Remote Sens. Lett.*, vol. 18, no. 9, pp. 1565-1569, Sept. 2021.
- [7] D. Wang, C. Zhao, Y. Song and T. Jin, "Crucial Region Search and Feature Discrimination for Radar-Based Human Activity Recognition," *IEEE Int. Things J.*, vol. 12, no. 17, pp. 36141-36154, Sept. 2025.
- [8] M. Ding, Z. Zhang, B. Tang, R. Liu and Y. Ding, "An Enhanced Radar Sensing Algorithm With Time-Frequency Spectrum Augmentation and Activity Recognition," *IEEE Int. Things J.*, vol. 12, no. 13, pp. 24996-25007, July 2025.
- [9] Z. Zheng, D. Zhang, X. Liang, X. Liu and G. Fang, "RadarFormer: End-to-End Human Perception With Through-Wall Radar and Transformers," *IEEE Trans. Neural Netw. Learning Syst.*, vol. 35, no. 12, pp. 18285-18299, Dec. 2024.
- [10] F. Qi, H. Lv, J. Wang and A. E. Fathy, "Quantitative Evaluation of Channel Micro-Doppler Capacity for MIMO UWB Radar Human Activity Signals Based on Time-Frequency Signatures," *IEEE Trans. Geosci. Remote Sens.*, vol. 58, no. 9, pp. 6138-6151, Sept. 2020.
- [11] C. Ding, J. Weng, H. Zhao, Q. Zhou, H. Hong and X. Zhu, "Omnidirectional Human Activity Recognition With Spatial-Temporal Trajectory-Based Compensation Using Monostatic MIMO Radar," *IEEE Trans. Microw. Theory Techniq.*, vol. 73, no. 8, pp. 5268-5280, Aug. 2025.

- [12] Y. Yang, Q. Mu, B. Li, Y. Ge, Q. Wang and Y. Lang, "Few-Shot Open-Set Gait Recognition Based on Radar Micro-Doppler Signatures," *IEEE Sensors J.*, vol. 25, no. 13, pp. 25134-25145, July 2025.
- [13] P. Miazek, A. Żmudzińska, P. karczmarek and A. Kiersztyn, "Human Behavior Analysis Using Radar Data: A Survey," *IEEE Access*, vol. 12, pp. 153188-153202, 2024.
- [14] T. Pardhu, V. Kumar, P. Kumar and N. Deevi, "Advancements in UWB-Based Human Motion Detection Through Wall: A Comprehensive Analysis," *IEEE Access*, vol. 12, pp. 89818-89835, 2024.
- [15] R. Shahbazian and I. Trubitsyna, "Human Sensing by Using Radio Frequency Signals: A Survey on Occupancy and Activity Detection," *IEEE Access*, vol. 11, pp. 40878-40904, 2023.
- [16] Y. Zhao, H. Zhou, S. Lu, Y. Liu, X. An, and Q. Liu, "Human Activity Recognition Based on Non-Contact Radar Data and Improved PCA Method," *Appl. Sci.*, vol. 12, no. 14, p. 7124, Jul. 2022.
- [17] A. D. Singh, S. S. Sandha, L. Garcia, and M. Srivastava, "RadHAR: Human Activity Recognition from Point Clouds Generated through a Millimeter-wave Radar," in *Proc. 3rd ACM Workshop Millimeter-Wave Netw. Sens. Syst.*, Los Cabos, Mexico, pp. 51-56, Oct. 2019.
- [18] C. Cheng, F. Ling, S. Guo, G. Cui, Q. Jian, C. Jia, and Q. Ran, "A real-time human activity recognition method for Through-the-Wall Radar," in *Proc. IEEE Radar Conf.*, Florence, Italy, Sep. 2020, pp. 1-5.
- [19] J. Zhu, H. Chen, and W. Ye, "A Hybrid CNN-LSTM Network for the Classification of Human Activities Based on Micro-Doppler Radar," *IEEE Access*, vol. 8, pp. 24713-24720, Feb. 2020.
- [20] R. El Hail, P. Mehrjousesht, D. M. M.-P. Schreurs, and P. Karsmakers, "Radar-Based Human Activity Recognition: A Study on Cross-Environment Robustness," *Electronics*, vol. 14, no. 5, p. 875, Feb. 2025.
- [21] T.-H. Tan, J.-H. Tian, A. K. Sharma, S.-H. Liu, and Y.-F. Huang, "Human Activity Recognition Based on Deep Learning and Micro-Doppler Radar Data," *Sensors*, vol. 24, no. 8, p. 2530, Apr. 2024.
- [22] M. Wang, Y. D. Zhang, and G. Cui, "Human Motion Recognition Exploiting Radar with Stacked Recurrent Neural Network," *Digit. Signal Process.*, vol. 87, pp. 125-131, Apr. 2019.
- [23] H. Li, A. Shrestha, H. Heidari, J. Le Kerneec, and F. Fioranelli, "Bi-LSTM Network for Multimodal Continuous Human Activity Recognition and Fall Detection," *IEEE Sensors J.*, vol. 20, no. 3, pp. 1533-1543, Feb. 2020.
- [24] F. M. Noori, M. Z. Uddin, and J. Torresen, "Ultra-Wideband Radar-Based Activity Recognition Using Deep Learning," *IEEE Access*, vol. 9, pp. 138132-138143, Oct. 2021.
- [25] A. Pesin, A. Louzir, and A. Haskou, "A novel approach for radar-based human activity detection and classification," in *Proc. IEEE Int. Conf. Consum. Electron.*, Las Vegas, NV, USA, pp. 1-4, Jan. 2021.
- [26] M. S. Seyfioglu, A. M. Ozbayoglu, and S. Z. Gurbuz, "Deep convolutional autoencoder for radar-based classification of similar aided and unaided human activities," *IEEE Trans. Aerosp. Electron. Syst.*, vol. 54, no. 4, pp. 1709-1723, Aug. 2018.
- [27] C. Ding, Y. Jia, G. Cui, C. Chen, X. Zhong, and Y. Guo, "Continuous human activity recognition through parallelism LSTM with multi-frequency spectrograms," *Remote Sens.*, vol. 13, no. 21, p. 4264, Oct. 2021.
- [28] M. Chakraborty, H. C. Kumawat, S. V. Dhavale, and A. A. B. Raj, "Application of DNN for radar micro-doppler signature-based human suspicious activity recognition," *Pattern Recognit. Lett.*, vol. 162, pp. 1-6, Oct. 2022.
- [29] J. Yan, X. Zeng, A. Zhou, and H. Ma, "MM-HAT: Transformer for Millimeter-Wave Sensing Based on Human Activity Recognition," in *Proc. IEEE Glob. Commun. Conf.*, Rio de Janeiro, Brazil, Dec. 2022, pp. 547-553.
- [30] K. Papadopoulos and M. Jelali, "A Comparative Study on Recent Progress of Machine Learning-Based Human Activity Recognition with Radar," *Appl. Sci.*, vol. 13, no. 23, p. 12728, Nov. 2023.
- [31] W. Gao, X. Yang, X. Qu, and T. Lan, "TWR-MCAE: a data augmentation method for through-the-wall radar human motion recognition," *IEEE Trans. Geosci. Remote Sens.*, vol. 60, pp. 1-17, Jan. 2022.
- [32] X. Qu, W. Gao, H. Meng, Y. Zhao, and X. Yang, "Indoor human behavior recognition method based on wavelet scattering network and conditional random field model," *IEEE Trans. Geosci. Remote Sens.*, vol. 61, pp. 1-15, Jan. 2023.
- [33] X. Yang, W. Gao, X. Qu, P. Yin, H. Meng, and A. E. Fathy, "A lightweight multiscale neural network for indoor human activity recognition based on macro and micro-Doppler features," *IEEE Int. Things J.*, vol. 10, no. 24, pp. 21836-21854, Aug. 2023.
- [34] X. Yang, W. Gao, X. Qu, Z. Ma, and H. Zhang, "Through-the-Wall radar human activity micro-doppler signature representation method based on joint Boulic-sinusoidal pendulum model," *IEEE Trans. Microw. Theory Tech.*, vol. 73, no. 2, pp. 1248-1263, Aug. 2024.
- [35] W. Gao, X. Qu, H. Meng, X. Sun, and X. Yang, "Adaptive micro-Doppler corner feature extraction method based on difference of gaussian filter and deformable convolution," *IEEE Signal Process. Lett.*, vol. 31, pp. 860-864, Jan. 2024.
- [36] X. Yang, W. Gao, X. Qu, and H. Meng, "Generalizable indoor human activity recognition method based on micro-Doppler corner point cloud and dynamic graph learning," *IEEE Trans. Aerosp. Electron. Syst.*, pp. 1-15, Jan. 2024.
- [37] W. Gao, "RADHARSimulator V1: Model-Based FMCW Radar Human Activity Recognition Simulator," *arXiv (Cornell University)*, Sep. 2025.
- [38] C. Lyu, W. Zhang, H. Huang, Y. Zhou, Y. Wang, Y. Liu, S. Zhang, and K. Chen, "RTMDet: An Empirical Study of Designing Real-Time Object Detectors," *arXiv (Cornell University)*, Dec. 2022.
- [39] Y. Chen, X. Yuan, J. Wang, R. Wu, X. Li, Q. Hou, and M.-M. Cheng, "YOLO-MS: Rethinking Multi-Scale Representation Learning for Real-Time Object Detection," *IEEE Trans. Pattern Anal. Mach. Intell.*, vol. 47, no. 6, pp. 4240-4252, Feb. 2025.
- [40] E. Gu, J. Zheng and H. Zhang, "3D Motion Parameters Fusion Under a Multi-Vision Motion Capture System," in *Proc. 2nd Int. Congr. Image Signal Process.*, Tianjin, China, pp. 1-4, 2009.
- [41] J. Wang, K. Sun, T. Cheng, B. Jiang, C. Heng, Y. Zhao, D. Liu, Y. Mu, M. Tan, X. Wang, W. Liu, and B. Xiao, "Deep High-Resolution Representation learning for visual recognition," *IEEE Trans. Pattern Anal. Mach. Intell.*, vol. 43, no. 10, pp. 3349-3364, Apr. 2020.
- [42] C. -H. Chen and D. Ramanan, "3D Human Pose Estimation = 2D Pose Estimation + Matching," in *Proc. IEEE Conf. Comput. Vis. Pattern Recognit.*, Honolulu, HI, USA, pp. 5759-5767, 2017.
- [43] C. Ionescu, D. Papava, V. Olaru and C. Sminchisescu, "Human3.6M: Large Scale Datasets and Predictive Methods for 3D Human Sensing in Natural Environments," *IEEE Trans. Pattern Anal. Mach. Intell.*, vol. 36, no. 7, pp. 1325-1339, July 2014.
- [44] T. Wu and X. Fan, "A Novel Gesture Recognition Model Under Sports Scenarios Based on Kalman Filtering and YOLOv5 Algorithm," *IEEE Access*, vol. 12, pp. 64886-64896, 2024.
- [45] I. Podkurkov, J. Zhang, A. F. Nadeev and M. Haardt, "Efficient Multidimensional Wideband Parameter Estimation for OFDM Based Joint Radar and Communication Systems," *IEEE Access*, vol. 7, pp. 112792-112808, 2019.
- [46] H. Arab, I. Ghaffari, L. Chioukh, S. O. Tatu and S. Dufour, "A Convolutional Neural Network for Human Motion Recognition and Classification Using a Millimeter-Wave Doppler Radar," *IEEE Sensors J.*, vol. 22, no. 5, pp. 4494-4502, March 2022.
- [47] R. Zhang, Z. Zhang, X. Zhang, Y. Tang, and W. Sheng, "Phase compensation transform for human detection with LFMCW radar," *Signal Process.*, vol. 172, p. 107565, Mar. 2020.
- [48] T. Jin and A. Yarovsky, "A Through-the-Wall radar imaging method based on a realistic model," *Int. J. Antennas Propag.*, vol. 2015, pp. 1-8, Jan. 2015.
- [49] X. Yang, H. Meng, X. Qu, W. Gao, and F. Liu, "Multipath ghost recognition and suppression method based on template matching for indoor human detection and location," *Intren. Things J.*, vol. 12, no. 14, pp. 27280-27290, Apr. 2025.
- [50] W. Gao, X. Qu and X. Yang, "Generalization Ability Analysis of Through-the-Wall Radar Human Activity Recognition," in *Proc. 2nd IEEE Int. Conf. Signal Inform. Data Process.*, Zhuhai, China, pp. 1-6, 2024.
- [51] K. Zhang, W. Zuo, Y. Chen, D. Meng and L. Zhang, "Beyond a Gaussian Denoiser: Residual Learning of Deep CNN for Image Denoising," *IEEE Trans. Image Process.*, vol. 26, no. 7, pp. 3142-3155, July 2017.
- [52] Y. Yu, Y. Ruan and J. Zhong, "AAV Parameters Estimation Based on Improved Time-Frequency Ridge Extraction and Hough Transform," *IEEE Access*, vol. 13, pp. 131074-131087, 2025.
- [53] I. Ullmann, R. G. Guendel, N. C. Kruse, F. Fioranelli and A. Yarovsky, "A Survey on Radar-Based Continuous Human Activity Recognition," *IEEE J. Microw.*, vol. 3, no. 3, pp. 938-950, July 2023.
- [54] X. Wang, S. Lai, Z. Chai, X. Zhang and X. Qian, "SPGNet: Serial and Parallel Group Network," *IEEE Trans. Multimedia*, vol. 24, pp. 2804-2814, 2022.
- [55] J. D. Bryan, J. Kwon, N. Lee, and Y. Kim, "Application of ultra-wide band radar for classification of human activities," *IET Radar Sonar Navig.*, vol. 6, no. 3, pp. 172-179, Feb. 2012.
- [56] X. Wang, G. Li, Y. Liu, and M. G. Amin, "Two-Level block matching pursuit for polarimetric Through-Wall radar imaging," *IEEE Trans. Geosci. Remote Sens.*, vol. 56, no. 3, pp. 1533-1545, Nov. 2017.

- [57] S. Ghorbani, K. Mahdaviyani, A. Thaler, K. Kording, D. J. Cook, G. Blohm, and N. F. Troje, "MoVi: A large multi-purpose human motion and video dataset," *PLoS ONE*, vol. 16, no. 6, pp. e0253157, Jun. 2021.
- [58] J. Liu, A. Shahroudy, M. Perez, G. Wang, L. -Y. Duan and A. C. Kot, "NTU RGB+D 120: A Large-Scale Benchmark for 3D Human Activity Understanding," *IEEE Trans. Pattern Anal. Mach. Intell.*, vol. 42, no. 10, pp. 2684-2701, Oct. 2020.
- [59] A. Zisserman, J. Carreira, K. Simonyan, W. Kay, B. Zhang, C. Hillier, S. Vijayanarasimhan, F. Viola, T. Green, T. Back, P. Natsev, and M. Suleyman, "The Kinetics Human Action Video Dataset," *arXiv (Cornell University)*, Mar. 2022.
- [60] S. Vishwakarma, W. Li, C. Tang, K. Woodbridge, R. Adve, and K. Chetty, "SimHumalator: an Open-Source End-to-End radar simulator for human activity recognition," *IEEE Aerosp. Electron. Syst. Mag.*, vol. 37, no. 3, pp. 6–22, Dec. 2021.
- [61] G. A. Sigurdsson, G. Varol, X. Wang, A. Farhadi, I. Laptev, and A. Gupta, "Hollywood in Homes: Crowdsourcing Data Collection for Activity Understanding," *Lect. Notes Comput. Sci.*, pp. 510–526, 2016.
- [62] H. Chen, X. Zhang, Y. Liu, and Q. Zeng, "Generative Adversarial networks capabilities for Super-Resolution reconstruction of weather Radar echo images," *Atmos.*, vol. 10, no. 9, p. 555, Sep. 2019.
- [63] S. S. Sumit, D. R. A. Rambli and S. Mirjalili, "Vision-Based Human Detection Techniques: A Descriptive Review," *IEEE Access*, vol. 9, pp. 42724-42761, 2021.
- [64] X. Yan, B. Liu and G. Qu, "Efficient Monocular Human Pose Estimation Based on Deep Learning Methods: A Survey," *IEEE Access*, vol. 12, pp. 72650-72661, 2024.
- [65] M. C. Motwani, M. C. Gadiya, and R. C. Motwani, "SURVEY ON IMAGE DENOISING TECHNIQUES," *Int. J. Adv. Eng. Res. Dev.*, vol. 4, no. 07, Jul. 2017.
- [66] Y. Gao, L. Cao, Z. Zhao, D. Wang, C. Fu, and Y. Guo, "Multiscale Residual Weighted Classification Network for Human Activity Recognition in Microwave Radar," *Sensors*, vol. 25, no. 1, pp. 197-221, 2025.
- [67] Z. Xu, H. Xu, W. Ai, Y. Yu, Y. Duan, R. Wang, X. Li, and P. Tian, "A Radar-Based Activity Recognition Approach Utilizing an Adaptive Masking Mechanism and Gated Units," *IEEE Trans. Aerosp. Electron. Syst.*, vol. 60, no. 5, pp. 1234–1245, May. 2025.
- [68] M. Chakraborty, H. C. Kumawat, S. V. Dhavale and A. B. Raj A., "DIAT-RadHARNet: A Lightweight DCNN for Radar Based Classification of Human Suspicious Activities," *IEEE Trans. Instrum. Meas.*, vol. 71, pp. 1-10, 2022.
- [69] X. Xiong, A. Ren, T. Yuan, and A. Zahid, "Human Motion Recognition by Micro-Doppler Features and Concatenated CNN-LSTM Network," *IEEE Sensors J.*, vol. 25, no. 7, pp. 12294-12302, Apr. 2025.
- [70] L. Tang, S. Guo, J. Li, J. Zhu, G. Cui, L. Kong, and X. Yang, "Through-Wall human activity Recognition based on adaptive Doppler feature enhancement," *IEEE Trans. Aerosp. Electron. Syst.*, vol. 61, no. 5, pp. 12970–12986, May 2025.
- [71] C. Li, X. Wang, J. Shi, H. Wang and L. Wan, "Residual Neural Network Driven Human Activity Recognition by Exploiting FMCW Radar," *IEEE Access*, vol. 11, pp. 111875-111887, 2023.
- [72] Y. Zhou, M. López-Benítez, L. Yu and Y. Yue, "Text2Doppler: Generating Radar Micro-Doppler Signatures for Human Activity Recognition via Textual Descriptions," *IEEE Sensors Lett.*, vol. 8, no. 10, pp. 1-4, Oct. 2024.